

Genome-wide modelling of transcription kinetics reveals patterns of RNA production delays

Antti Honkela¹, Jaakko Peltonen^{2,3}, Hande Topa², Iryna Charapitsa⁴, Filomena Matarese⁵, Korbinian Grote⁶, Hendrik G. Stunnenberg⁵, George Reid⁴, Neil D. Lawrence⁷, and Magnus Rattray⁸

¹Helsinki Institute for Information Technology HIIT, Department of Computer Science, University of Helsinki, Finland

²Helsinki Institute for Information Technology HIIT, Department of Computer Science, Aalto University, Espoo, Finland

³School of Information Sciences, University of Tampere, Finland

⁴Institute for Molecular Biology, Mainz, Germany

⁵Nijmegen Centre for Molecular Life Sciences, Radboud University Nijmegen, NL

⁶Genomatix Software GmbH, Muenchen, Germany

⁷Department of Computer Science, University of Sheffield, UK

⁸Faculty of Life Sciences, University of Manchester, UK

July 31, 2018

Abstract

Genes with similar transcriptional activation kinetics can display very different temporal mRNA profiles due to differences in transcription time, degradation rate and RNA processing kinetics. Recent studies have shown that a splicing-associated RNA production delay can be significant. To investigate this issue more generally it is useful to develop methods applicable to genome-wide data sets. We introduce a joint model of transcriptional activation and mRNA accumulation which can be used for inference of transcription rate, RNA production delay and degradation rate given data from high-throughput sequencing time course experiments. We combine a mechanistic differential equation model with a non-parametric statistical modelling approach allowing us to capture a broad range of activation kinetics, and use Bayesian parameter estimation to quantify the uncertainty in the estimates of the kinetic parameters. We apply the model to data from estrogen receptor (ER- α) activation in the MCF-7 breast cancer cell line. We use RNA polymerase II (pol-II) ChIP-Seq time course data to characterise transcriptional activation and mRNA-Seq time course data to quantify mature transcripts. We find that 11% of genes with a good signal in the data display a delay of more than 20 minutes between completing transcription and mature mRNA production. The genes displaying these long delays are significantly more likely

to be short. We also find a statistical association between high delay and late intron retention in pre-mRNA data, indicating significant splicing-associated production delays in many genes.

1 Introduction

Induction of transcription through extracellular signalling can yield rapid changes in gene expression for many genes. Establishing the timing of events during this process is important for understanding the rate-limiting mechanisms regulating the response and vital for inferring causality of regulatory events. Several processes influence the patterns of mRNA abundance observed in the cell, including the kinetics of transcriptional initiation, elongation, splicing and mRNA degradation. It was recently demonstrated that significant delays due to the kinetics of splicing can be an important factor in a focussed study of genes induced by Tumor Necrosis Factor (TNF- α) [1]. Delayed transcription can play an important functional role in the cell; for example, inducing oscillations within negative feedback loops [2] or facilitating "just-in-time" transcriptional programmes with optimal efficiency [3]. It is therefore important to identify such delays and to better understand how they are regulated. In this contribution we combine RNA polymerase (pol-II) ChIP-Seq data with RNA-Seq data to study transcription kinetics of estrogen receptor signalling in breast cancer cells. Using an unbiased genome-wide modelling approach we find evidence for large delays in mRNA production in 11% of the genes with a quantifiable signal in our data. A statistical analysis of genes exhibiting large delays indicates that splicing kinetics is a significant factor and can be the rate-limiting step for gene induction.

A high-throughput sequencing approach is attractive as it gives broad coverage and thus allows us to uncover the typical properties of the system. However, high-throughput data are associated with significant sources of noise and the temporal resolution of our data is necessarily reduced compared to previous studies using more focussed PCR-based assays [1, 4]. We have therefore developed a statistically efficient model-based approach for estimating the kinetic parameters of interest. We use Bayesian estimation to provide a principled assessment of the uncertainty in our inferred model parameters. Our model can be applied to all genes with sufficiently strong signal in both the mRNA and pol-II data with only mild restrictions on the shape of the transcriptional activation profile (1814 genes here).

A number of other works studying transcription and splicing dynamics (e.g. [1, 5, 6]) forgo detailed dynamical modelling, which limits their ability to properly account for varying mRNA half-lives. Our statistical model incorporates a linear ordinary differential equation of transcription dynamics, including mRNA degradation. Similar linear differential equation models have been proposed as models of mRNA dynamics previously [4, 7, 8], but assuming a specific parametric form for the transcriptional activity. In contrast, we apply a non-parametric Gaussian process framework that can accommodate a quite general shape of transcriptional activity. As demonstrated previously [9–11], the linearity of the

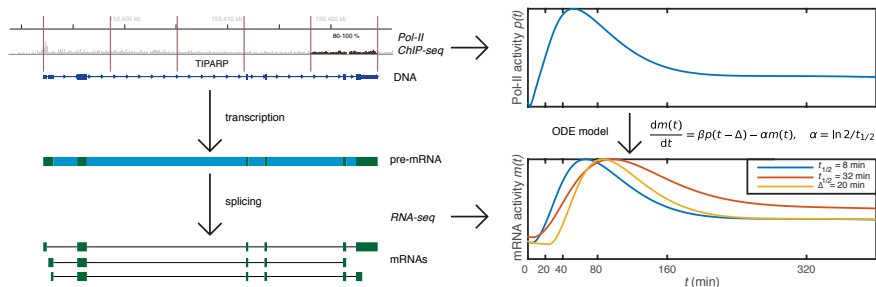


Figure 1: A cartoon illustrating the underlying biology and data gathering at a single time point (left) and time series modelling (right). The data come from pol-II ChIP-seq, summarised over the last 20% of the gene body, and RNA-seq computationally split to pre-mRNA and different mRNA transcript expression levels. The modelling on the right shows the effect of changing mRNA half-life ($t_{1/2}$) or RNA production delay (Δ) on the model response: both induce a delay on the mRNA peak relative to the pol-II peak, but the profiles have otherwise distinct shapes.

differential equation allows efficient exact Bayesian inference of the transcriptional activity function. Before presenting our results we outline our modelling approach.

2 Model-based inference of transcriptional delays

Our modelling approach is summarised in Fig. 1. We model the dynamics of transcription using a linear differential equation,

$$\frac{dm(t)}{dt} = \beta p(t - \Delta) - \alpha m(t), \quad (1)$$

where $m(t)$ is the mature mRNA abundance and $p(t)$ is the transcription rate at the 3' end of the gene at time t which is scaled by a parameter β since we do not know the scale of our $p(t)$ estimates. The parameter Δ captures the delay between transcription completion and mature mRNA production. We refer to this as the RNA production delay, defined as the time required for the polymerase to disengage from the pre-mRNA and be fully processed into a mature transcript. The parameter α is the mRNA degradation rate which determines the mRNA half-life ($t_{1/2} = \ln 2 / \alpha$). We infer all model parameters (α , β , Δ , the noise variance and parameters of the Gaussian process covariance function discussed below) using a Markov chain Monte Carlo (MCMC) procedure. The posterior distribution of the model parameters quantifies our uncertainty and we use percentiles of the posterior distribution when reporting credible regions around the mean or median values.

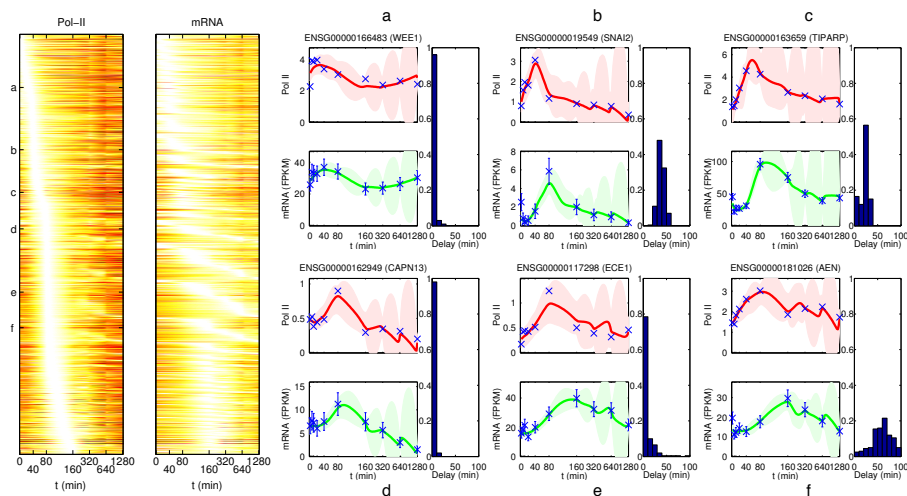


Figure 2: Left: Heat map of inferred pol-II and mRNA activity profiles after MCF7 cells are stimulated with estradiol. Genes with sufficient signal for modelling are sorted by the time of peak pol-II activity in the fitted model. Right: Examples of fitted model for six genes. For each gene, we show the fit using the pol-II ChIP-Seq data (collected from the final 20% of the transcribed region) representing the transcriptional activity $p(t)$ (see Eqn. (1)), and using the RNA-seq data to represent gene expression $m(t)$. Solid red/green lines show the mean model estimates for the pol-II/mRNA profiles respectively with associated credible regions. In each case we show the posterior distribution for the inferred delay parameter Δ to the right of the temporal profiles. Note that the final measurement times are very far apart (the x -axis is compressed to aid visualisation) leading to high uncertainty in the model fit at late times. However, this does not significantly affect the inference of delays for early induced genes.

We measure the transcriptional activity $p(t)$ using RNA polymerase (pol-II) ChIP-Seq time course data collected close to the 3' end of the gene (reads lying in the last 20% of the transcribed region). Our main assumption is that pol-II abundance at the 3' end of the gene is proportional to the production rate of mature mRNA after a possible delay Δ due to disengaging from the polymerase and processing. The mRNA abundance is measured using RNA-Seq reads mapping to annotated transcripts, taking all annotated transcripts into account and resolving mapping ambiguities using a probabilistic method [12] (see Methods Section for details). As we limit our analysis to pol-II data collected from the 3'-end of the transcribed region, we do not expect a significant contribution to Δ from transcriptional delays when fitting the model. Such transcriptional delays have recently been studied by modelling transcript elongation dynamics using pol-II ChIP-Seq time course data [13] and nascent mRNA (GRO-Seq) data [14] in the same system. Here we instead focus on production delays that can occur

after elongation is essentially complete.

Existing approaches to fitting models of this type have assumed a parametric form for the activation function $p(t)$ [4, 7, 8]. We avoid restricting the function shape by using a non-parametric Bayesian procedure for fitting $p(t)$. We model $p(t)$ as a function drawn from a Gaussian process which is a distribution over functions. The general properties of functions drawn from a Gaussian process prior are determined by a *covariance function* which can be used to specify features such as smoothness and stationarity. We choose a covariance function that ensures $p(t)$ is a smooth function of time since our data are averaged across a cell population. Our choice of covariance function is non-stationary and has the property that the function has some persistence and therefore tends to stay at the same level between observations (see Supplementary Material for further details). The advantage of using a non-parametric approach is that we only have to estimate a small number of parameters defining the covariance function (two in this case, defining the amplitude and time-scale of the function). If we were to represent $p(t)$ as a parametrised function we would have to estimate a larger number of parameters to describe the function with sufficient flexibility. The Bayesian inference procedure we use to associate each estimated parameter with a credible region would be more challenging with the inclusion of these additional parameters.

We have previously shown how to perform inference over differential equations driven by functions modelled using Gaussian processes [9–11]. The main methodological novelty in the current work is the inclusion of the delay term in equation (1) and the development of a Bayesian inference scheme for this and other model parameters. In brief, we cast the problem as Bayesian inference with a Gaussian process prior distribution over $p(t)$ that can be integrated out to obtain the data likelihood under the model in Eqn. (1) assuming Gaussian observation noise. This likelihood function and its gradient are used for inference with a Hamiltonian MCMC algorithm [15] to obtain a posterior distribution over all model parameters and the full pol-II and mRNA functions $p(t)$ and $m(t)$.

3 Results

We model the transcriptional response of MCF-7 breast cancer cells after stimulation by estradiol to activate estrogen receptor (ER- α) signalling. Fig. 2 shows the inferred pol-II and mRNA profiles for all genes with sufficient signal for modelling, along with some specific examples of fitted models and estimated delay parameters. Before discussing these results further below, we describe the application of our method to realistic simulated data to assess the reliability of our approach for parameter estimation under a range of conditions.

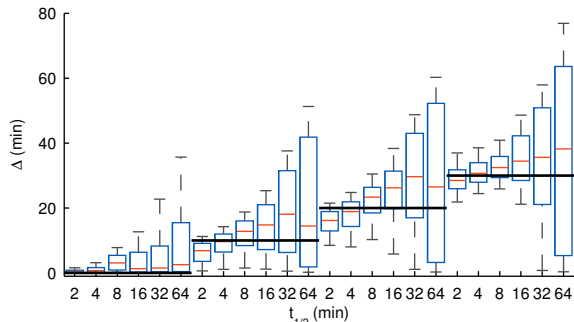


Figure 3: Boxplots of parameter posterior distributions illustrating parameter estimation performance on synthetic data for the delay parameter Δ . The strong black lines indicate the ground truth used in data generation. The box extends from 25th to 75th percentile of the posterior distribution while the whiskers extend from 9th to 91st percentile. The results show that delay estimates are accurate and reliable, with the true value always in the high posterior density region.

3.1 Simulated data

We applied our method to data simulated from the model in Eqn. (1) using a $p(t)$ profile inferred using pol-II data from the TIPARP gene (gene c in Fig. 2; see Supplementary Material for further details over the simulated data). We simulated data using different values of α and Δ to test whether we can accurately infer the delay parameter Δ . Fig. 3 shows the credible regions of Δ for different ground truth levels (horizontal lines) and for different mRNA degradation rates (half-lives given on the x -axis). The results show that Δ can be confidently inferred with the ground truth always lying within the central part of the credible region. The maximum error in posterior median estimates is less than 10 min and when positive, the true value is always above the 25th percentile of the posterior. We observed that as the mRNA half-life increases, our confidence in the delay estimates is reduced. This is because the mRNA integrates the transcriptional activity over time proportional to the half-life leading to a more challenging inference problem. We also note that inference of the degradation parameter α is typically more difficult than inference of the delay parameter Δ (see Fig. S1). However, a large uncertainty in the inferred degradation rate does not appear to adversely affect the inference of the delay parameters which are the main focus here. More time-points, or a different spacing of time points, would be needed to accurately infer the degradation rates. Additional results of delay estimation in a scenario where the simulated half-life changes during the time course are presented in Fig. S2. These results demonstrate that the obtained delay estimates are reliable even in this scenario.

3.2 Estrogen receptor signalling

We applied our method to RNA-Seq and pol-II ChIP-Seq measurements from MCF-7 cells stimulated with estradiol to activate ER- α signalling (see Methods section). The measurements were taken from cells extracted from the same population to ensure that time points are directly comparable across technologies. Example fits of our model are shown in Fig. 2. The examples show a number of different types of behaviour ranging from early induced (a-c) to late induced (d-f), and from very short delay (a, d, e) to longer delays (b, c, f). Example (e), ECE1, is illuminating because visual inspection of the profiles suggests a possible delay, but a more likely explanation according to our model is a longer mRNA half-life and the posterior probability of a long delay is quite low. Indeed, it is well known that differences in stability can lead to delayed mRNA expression [16] and therefore delays in mRNA expression peak relative to pol-II peak time are not sufficient to indicate a production delay. Changes in splicing can be another potential confounder, but our transcript-based analysis of RNA-seq data can account for that. An example of how more naive RNA-seq analysis could fail here is presented in Fig. S3.

The parameter estimates of the models reveal a sizeable set of genes with strong evidence of long delays between the end of transcription and production of mature mRNA. We were able to obtain good model fits for 1864 genes. We excluded 50 genes with posterior median delay ≥ 120 min, as these are unreliable due to sparse sampling late in the time course, which is apparent from broad delay posterior distributions. Out of the remaining 1814 genes with reliable estimates, 204 (11%) had a posterior median delay larger than 20 min between pol-II activity and mRNA production while 98 genes had the 25th percentile of delay posterior larger than 20 min, indicating confident high delay estimates. A histogram of median delays is shown in Fig. 4 (left). The 120 min long delay cut-off was selected by visual observation of model fits which were generally reasonable for shorter delays. Note that late time points in our data set are highly separated due to the exponential time spacing used and thus the model displays high levels of uncertainty between these points (see Fig. 2). Therefore genes displaying confident delay estimates are typically early-induced such that time points are sufficiently close for a confident inference of delay time. Our Bayesian framework makes it straightforward to establish the confidence of our parameter estimates.

3.3 Genomic features associated with long-delay genes

Motivated by previous studies [5, 6, 17] we investigated statistical association between the observed RNA production delay and genomic features related to splicing. We found that genes with a short pre-mRNA (Fig. 5, left panel) are more likely to have long delays. We also find that genes where the ratio of the last intron's length in the longest annotated transcript over the total length of the transcript is large (Fig. 5, right panel) are also more likely to have long delays, but this effect appears to be weaker. These two genomic features, short

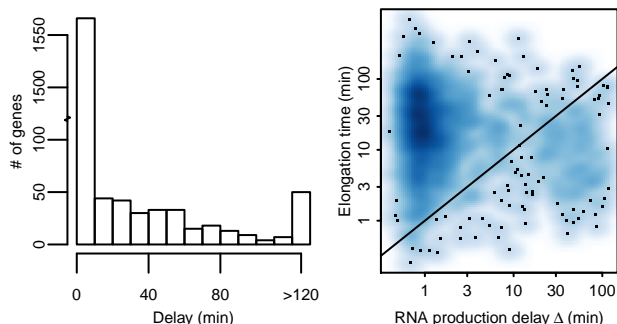


Figure 4: Left: A histogram of delay posterior medians from 1864 genes found to fit the model well. Estimated delays larger than 120 min are considered unreliable and are grouped together. These 50 genes were excluded from further analysis, leaving 1814 genes for the main analysis. Right: Estimated gene transcriptional delay for the longest transcript plotted against the estimated posterior median RNA production delay. The transcriptional delay is estimated assuming each gene follows the median transcriptional velocity measured in Ref. [14]. The solid line corresponds to equal delays.

pre-mRNA and relatively long last introns, are positively correlated, making it more difficult to separate their effects. To do so, Fig. S6 shows versions of the right panel of Fig. 5 but only including genes with pre-mRNAs longer than 10 kb or 30 kb. The number of genes with long last introns in these sets is smaller and the resulting p -values are thus less extreme, but the general shape of the curves is the same. We did not find a significant relationship with the absolute length of the last intron. This may be because the two observed effects would tend to cancel out in such cases. We also checked if exon skipping is associated with long delays as previously reported [6]. The corresponding results in Fig. S7 show no significant difference in estimated delays in genes with and without annotated exon skipping.

3.4 Analysis of the intronic read and pol-II distribution

We investigated whether there was evidence of differences in the pattern of splicing completion for long-delay genes. To quantify this effect, we developed a pre-mRNA end accumulation index: the ratio of intronic reads in the last 50% of the pre-mRNA to the intronic reads in the first 50% at late (80-320 min) and early (10-40 min) times. Fig. 6 shows that genes with a long estimated delay display an increase in late intron retention at the later times. There is a statistically significant difference in the medians of index values for short and long delay genes ($p < 0.01$, Wilcoxon's rank-sum test p -values for different short/long delay splits are shown in Fig. 6). The example on the left of Fig. 6, DLX3, is a relatively short gene of about 5 kb and thus differences over time cannot be explained by the time required for transcription to complete. The

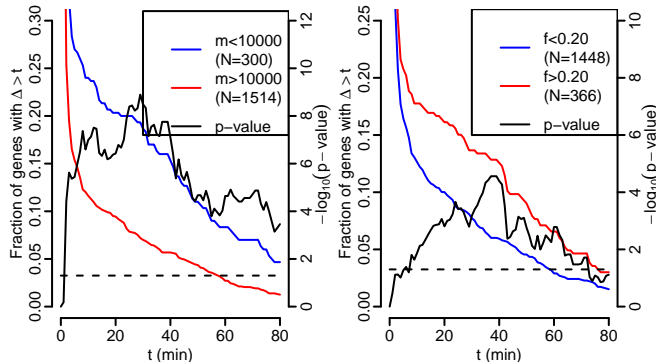


Figure 5: Tail probabilities for delays. Left: genes whose longest pre-mRNA transcript is short (m is the length from transcription start to end). Right: genes with relatively long last introns (f is the ratio of the length of the last intron of the longest annotated transcript of the gene divided by the length of that transcript pre-mRNA). The fraction of genes with long delays Δ is shown by the red and blue lines (left-hand vertical axis). In both subplots, the black curve denotes the p -values of Fisher’s exact test for equality of fractions depicted by the red and blue curves conducted separately at each point (right-hand vertical axis) with the dashed line denoting $p < 0.05$ significance threshold. Similar plots for other values of m and f as well as different gene filter setups are given in Figs. S4–S5.

corresponding analysis for pol-II ChIP-seq reads as well as GRO-seq reads is in Fig. S8. It shows a clear delay-associated accumulation to the last 5% nearest to the 3’ end, while for pol-II in the last 50% the accumulation is universal. These results suggest our short delay genes tend to be efficiently spliced while long delay genes are more likely to exhibit delayed splicing towards the 3’ end. There is also evidence of some accumulation of pol-II near the 3’ end although the effect appears relatively weak. We note that Grosso *et al.* [18] identified genes with elevated pol-II at the 3’-end which were found to be predominantly short, consistent with our set of delayed genes, and with nucleosome occupancy consistent with pausing at the 3’ end.

3.5 Relative importance of production and elongation delays

To better understand what are the rate-limiting steps in transcription dynamics, we assessed the relative importance of the observed RNA production delays in comparison to transcriptional delays due to elongation time. We estimated elongation times for each gene using assumed transcriptional velocity corresponding to the 2.1 kb/min median estimate from [14] combined with the length of the longest annotated pre-mRNA transcript. Others (e.g. [13]) have reported higher

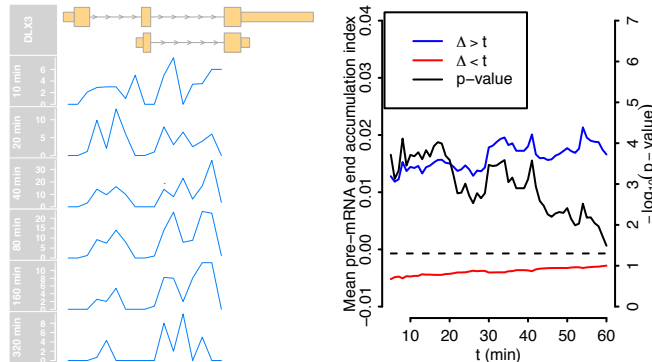


Figure 6: Left: We show the density of RNA-Seq reads uniquely mapping to the introns in the DLX3 gene, summarised in 200 bp bins. The gene region is defined from first annotated transcription start until the end of last intronic read. The ratio of the number of intronic reads after and before the midpoint of the gene region is used to quantify the 3' retention of introns. The pre-mRNA end accumulation index is the difference between averages of this ratio computed over late times (80-320 min) and early times (10-40 min). Right: Differences in the mean pre-mRNA accumulation index (left-hand vertical axis) in long delay genes (blue) and short delay genes (red) as a function of the cut-off used to distinguish the two groups (horizontal axis). Positive values indicate an increase in 3' intron reads over time. The black line shows the p -values of Wilcoxon's rank sum test between the two groups at each cut-off (right-hand vertical axis).

velocities, so this approach should provide reasonable upper bounds on actual elongation time for most genes. A comparison of these delays with our posterior median delay estimates is shown in Fig. 4 (right). The figure shows the majority of genes with short production delays and moderate elongation time in the top-left corner of the figure, but 14.3% (260/1814) of genes have a longer RNA production delay than elongation time.

4 Discussion

Through model-based coupled analysis of pol-II and mRNA time course data we uncovered the processes shaping mRNA expression changes in response to estrogen receptor signalling. We find that a large number of genes exhibit significant production delays. We also find that delays are associated with short overall gene length, relatively long final intron length and increasing late-intron retention over time. Our results support a major role for splicing-associated delays in shaping the timing of gene expression in this system. Our study complements the discovery of similarly large splicing-associated delays in a more focussed study of TNF-induced expression [1] indicating that splicing delays are

likely to be important determinants of expression dynamics across a range of signalling pathways.

It is known that splicing can strongly influence the kinetics of transcription. Khodor *et al.* carried out a comparative study of splicing efficiency in fly and mouse and found a positive correlation between absolute gene length and splicing efficiency [5]. This suggests that efficient co-transcriptional splicing is facilitated by increased gene length and is consistent with our observation that delays are more common in shorter genes. In these genes it appears that the mature mRNA cannot be produced after transcription until splicing is completed; it is splicing rather than transcription that is the rate-limiting step for these genes. In the same study it was also observed that introns close to the 3'-end of a gene are less efficiently spliced which is consistent with our observation that the relative length of the final intron may impact on splicing delays. A further theoretical model supporting a link between long final introns and splicing inefficiency was recently suggested in Ref. [19], but it is unclear if it can fully explain the observed relationships.

Our model assumes a constant mRNA degradation rate which may be unrealistic. Given the difficulty of estimating even a single constant degradation rate for simulated data where the true rate is constant, it seems infeasible to infer time-varying rates with the current data. On the other hand, estimated delays were quite reliably inferred even when we simulated data with a time-varying degradation rate (Fig. S2), and hence the potentially incorrect degradation model should not affect the main results significantly.

It is important to differentiate the delays found here with transcriptional delays required for pol-II elongation to complete. Elongation time can be a significant factor in determining the timing of gene induction and elongation dynamics has been modelled using both pol-II ChIP-Seq [13] and nascent RNA (GRO-Seq) [14] time course measurements in the system considered here. However, in this study we limited our attention to pol-II data at the 3'-end of the gene, i.e. measuring polymerase density changes in the region where elongation is almost completed. Therefore, we will not see transcription delays in our data and the splicing-associated delays discussed above are not related to elongation time. Indeed, the splicing-associated delays observed here are more likely to affect shorter genes where transcription completes rapidly. These splicing-associated delays are much harder to predict from genomic features than transcriptional delays, which are mainly determined by gene length, although we have shown an association with final intron length and gene length. In the future it would be informative to model data from other systems to establish associations with system-specific variables (e.g. alternative splice-site usage) and thereby uncover context-specific mechanisms regulating the delays that we have observed here.

4.1 Availability

Raw data are available at GEO (accession GSE62789). A browser of all model fits and delay estimates is available at <http://ahonkela.users.cs.helsinki.fi/pol2rna/>. Code for reproducing the experiments is available at

<https://github.com/ahonkela/pol2rna>.

5 Methods

5.1 Data acquisition and mapping

MCF-7 breast cancer cells were stimulated with estradiol (E2) after being placed in estradiol free media for three days, similarly as previously described [13]. We measured pol-II occupancy and mRNA concentration from the same cell population collected at 10 time points on a logarithmic scale: 0, 5, 10, 20, 40, 80, 160, 320, 640 and 1280 min after E2 stimulation. At each time point, the pol-II occupancy was measured genome-wide by ChIP-seq and mRNA concentration using RNA-Seq. Raw reads from the ChIP-Seq data were mapped onto the human genome reference sequence (NCBI_build37) using the Genomatix Mining Station (software version 3.5.2; further details in Supplementary Material). On average 84.0% of the ChIP-Seq reads were mapped uniquely to the genome. The RNA-seq reads were mapped using bowtie to a transcriptome constructed from Ensembl version 68 annotation allowing at most 3 mismatches and ignoring reads with more than 100 alignments. The transcriptome was formed by combining the cDNA and ncRNA transcriptomes with pre-mRNA sequences containing the full genomic sequence from the beginning of the first annotated exon to the end of the last annotated exon. On average 84.7% of the RNA-seq reads were mapped.

5.2 RNA-seq data processing

mRNA concentration was estimated from RNA-seq read data using BitSeq [12]. BitSeq is a probabilistic method to infer transcript expression from RNA-seq data after mapping to an annotated transcriptome. We estimated expression levels to all entries in the transcriptome, including the pre-mRNA transcripts, and used the sum of the mRNA transcript expressions in FPKM units to estimate the mRNA expression level of a gene. Different time points of the RNA-seq time series were normalised using the method of [20].

5.3 Pol-II ChIP-seq data processing

The ChIP-seq data were processed into time series summarising the pol-II occupancy at each time point for each human gene. We considered the last 20% of the gene body nearest to the 3'-end. The gene body was defined from the start of the first exon to the end of the last exon in Ensembl 68 annotation. The data were subject to background removal and normalisation of time points. (Full details in the Supplementary Material.)

5.4 Filtering of active genes

We removed genes with no clear time-dependent activity by fitting time-dependent Gaussian process models to the activity curves and only keeping genes with Bayes factor at least 3 in favour of the time-dependent model compared to a null model with no time dependence. We also removed genes that had no pol-II observations at 2 or more time points. This left 4420 genes for which we fitted the models.

5.5 Modelling and parameter estimation

We model the relationship between pol-II occupancy and mRNA concentration using the differential equation in Eqn. (1) which relates the pol-II time series $p(t)$ and corresponding mRNA time series $m(t)$ for each gene. We model $p(t)$ in a nonparametric fashion by applying a Gaussian Process (GP) prior over the shapes of the functions. We slightly modify the model in Eqn. (1) by adding a constant β_0 to account for the limited depth of pol-II ChIP-Seq measurements,

$$\frac{dm(t)}{dt} = \beta_0 + \beta p(t - \Delta) - \alpha m(t) \quad (2)$$

This differential equation can be solved for $m(t)$ as a function of $p(t)$ in closed form. The pol-II concentration function $p(t)$ is represented as a sample from a GP prior which can be integrated out to compute the data likelihood. The model can be seen as an extension of a previous model applied to transcription factor target identification [11]. Unlike Ref. [11], we model $p(t)$ as a GP defined as an integral of a function having a GP prior with RBF covariance, which implies that $p(t)$ tends to remain constant between observed data instead of reverting back to the mean. Additionally we introduce the delay between pol-II concentration and mRNA production as well as model the initial mRNA concentration as an independent parameter. In the special case where $\Delta = 0$, and $m_0 = \beta_0/\alpha$, Eqn. (S3) reduces to the previous model (Eqn. 4 in [11]). In order to fit the model to pol-II and mRNA time course data sampled at discrete times, we assume we observe $m(t)$ and $p(t)$ corrupted by zero-mean Gaussian noise independently sampled for each time point. We assume the pol-II noise variance is a constant σ_p^2 and infer it as a parameter of the model. The mRNA noise variances for each time point are sums of a shared constant σ_m^2 and a fixed variance inferred by BitSeq by combining the technical quantification uncertainty from BitSeq expression estimation with an estimate of biological variance from the BitSeq differential expression model (full details in Supplementary Material).

Given the differential equation parameters, GP inference yields a full posterior distribution over the shape of the Pol-II and mRNA functions $p(t)$ and $m(t)$. We infer the differential equation parameters from the data using MCMC sampling which allows us to assign a level of uncertainty to our parameter estimates. To infer a full posterior over the differential equation parameters β_0 , β , α , Δ , m_0 , $E[p_0] = \mu_p$, the observation model parameters σ_p^2 , σ_m^2 , and a magnitude parameter C_p and width parameter l of the GP prior, we set near-flat priors for them over reasonable value ranges, except for the delay Δ whose

prior is biased toward 0 (exact ranges and full details are presented in Supplementary Material). We combine these priors with the likelihood obtained from the GP model after marginalising out $p(t)$ and $m(t)$, which can be performed analytically. We infer the posterior over the parameters by Hamiltonian MCMC sampling. This full MCMC approach utilises gradients of the distributions for efficient sampling and rigorously takes uncertainty over differential equation parameters into account. Thus the final posterior accounts for both the uncertainty about differential equation parameters, and uncertainty over the underlying functions for each differential equation. We ran 4 parallel chains starting from different random initial states for convergence checking using the potential scale reduction factor of [21]. We obtained 500 samples from each of the 4 chains after discarding the first half of the samples as burn-in and thinning by a factor of 10. Posterior distributions over the functions $p(t)$ and $m(t)$ are obtained by sampling 500 realisations of $p(t)$ and $m(t)$ for each parameter sample from the exact Gaussian conditional posterior given the parameters in the sample. The resulting posteriors for $p(t)$ and $m(t)$ are non-Gaussian, and are summarised by posterior mean and posterior quantiles. Full details of the MCMC procedure are in Supplementary Material.

5.6 Filtering of results

Genes satisfying the following conditions were kept for full analysis. (Full implementation details of each step are in Supplementary Material.)

1. $p(t)$ has the maximal peak in the densely sampled region between 1 min and 160 min.
2. Estimated posterior median delay is less than 120 min.
3. $p(t)$ does not change too much before $t = 0$ min to match the known start in steady state.

5.7 Analysis of the gene annotation features associated with the delays

Ensembl version 68 annotations were used to derive features of all genes. For each annotated transcript, we computed the total pre-mRNA length m as the distance from the start of the first exon to the end of the last exon, and the lengths of all the introns. Transcripts consisting only of a single exon (and hence no introns) were excluded from further analysis. For each gene, we identified the transcript with the longest pre-mRNA and used that as the representative transcript for that gene. The last intron share f was defined as the length of the last intron of the longest transcript divided by m .

5.8 Pre-mRNA end accumulation index

For this analysis, we only considered reads aligning uniquely to pre-mRNA transcripts and not to any mRNA transcripts. We counted the overlap of reads

with 200 bp bins starting from the beginning of the first exon of each gene ending with the last non-empty bin. We compute the fraction $r_{e,i}$ of all reads in the latter half of bins in each sample i , and define the index as the difference of the means of $r_{e,i}$ over late time points (80-320 min) and over early time points (10-40 min).

Acknowledgments

The work was funded by the European ERASysBio+ initiative project “Systems approach to gene regulation biology through nuclear receptors” (SYNERGY) by the BBSRC (BB/I004769/2 to JP, MR and NDL), Academy of Finland (135311 to AH and HT) and by the BMBF (grant award ERASysBio+ P#134 to GR; grant no. 0315715B to KG). MR, NDL and KG were further supported by EU FP7 project RADIANT (grant no. 305626), and AH and JP by the Academy of Finland (grant nos. 252845, 259440, 251170).

Supplementary material

In the following we provide details of data acquisition, processing of RNA-seq data and filtering of active genes, processing of pol-II ChIP-seq data, differential equation modelling of the connection between pol-II and mRNA, Gaussian process based inference of underlying time series, and summarisation and filtering of results. We then provide an explanation of how synthetic data were used to study accuracy of parameter estimation for mRNA half life, a measure of mRNA decay in the differential equation model between pol-II and mRNA. Lastly, we provide additional figures about tail probabilities of delays for alternative result filtering choices, an additional figure about long posterior mean delays with and without annotated exon skipping, and differences in pre-mRNA accumulation in short and long delay genes.

A Data acquisition

MCF-7 breast cancer cells were treated with estradiol (E2). The cells were put in estradiol free media for three days. This is defined media devoid of phenol red (which is estrogenic) containing 2% charcoal stripped foetal calf serum. The charcoal absorbs estradiol but not other essential serum components, such as growth factors. This resulted in basal levels of transcription from E2 dependent genes. The cells were then incubated with E2 containing media, which resulted in the stimulation of estrogen responsive genes. Measurements were taken at logarithmically spaced time points 0, 5, 10, 20, ..., 1280 minutes after E2 stimulation.

At each time point, the pol-II occupancy was measured genome-wide by ChIP-seq. Raw reads were mapped onto the human genome reference sequence (NCBI_build37) using the Genomatix Mining Station (software version 3.5.2). The mapping software is an index-based mapper using a shortest unique subword index generated from the reference to identify possible read positions. A subsequent alignment step is then used to get the highest-scoring match(es) according to the parameters used. We used a minimum alignment quality threshold of 92% for mapping, reads were not trimmed. On average 84% percent of reads could be mapped uniquely.

At each time point, the pre-mRNA and mature mRNA abundances were measured for each human gene by RNA-seq. Total RNA was isolated and subjected to rRNA depletion with the Ribo-Zero Magnetic Gold Kit and processed further for strand-specific RNA-seq. The RNA-seq reads were mapped using Bowtie to a transcriptome constructed from Ensembl version 68 annotation allowing at most 3 mismatches and ignoring reads with more than 100 alignments. The transcriptome was formed by combining the cDNA and ncRNA transcriptomes with pre-mRNA sequences containing the full genomic sequence from the beginning of the first annotated exon to the end of the last annotated exon. On average 84.7% of the RNA-seq reads were mapped.

All the ChIP-seq and RNA-seq data are available from the NCBI Gene

Expression Omnibus under accession number GSE62789.

B RNA-seq data processing

RNA-seq data were analysed at each time point separately using BitSeq [12]. The reads were first mapped to human reference transcriptome (Ensembl v68) using Bowtie version 0.12.7 [22]. In order to separate pre-mRNA activity as well, we augmented the reference transcriptome with pre-mRNA transcripts for each gene that consisted of the genomic sequence from the beginning of the first exon to the end of the last exon of the gene.

BitSeq uses a probabilistic model to probabilistically assign multimapping reads to transcript isoforms [12], in our case also including the pre-mRNA transcripts. We obtained gene expression estimates by adding the corresponding mRNA transcript expression levels. In addition to the mean expression levels, BitSeq provides variances of the transcript isoform expression levels. We further used the biological variance estimation procedure from BitSeq differential expression analysis on the estimated gene expression levels by treating the first three time points (0, 5, 10 min) as biological replicates. Genes with similar mean expression levels (log-RPKM) were grouped together such that each group contained 500 genes except for the last group with 571 genes with the highest expression. Then, the biological variances were estimated for each group of genes by using the Metropolis–Hastings algorithm used in BitSeq stage 2 [12]. Biological variances for the single measurements were determined according to the gene expression levels at each time point, where each gene was considered to belong to the closest gene group according to its expression level. The observation noise variance for each observation was defined as the sum of the technical (BitSeq stage 1) and biological (BitSeq stage 2) variances, and transformed from log-expression to raw expression using

$$\sigma_{\text{raw}}^2 = \sigma_{\text{log}}^2 \exp(\mu_{\text{log}})^2. \quad (\text{S1})$$

Different time points of the RNA-seq time series were normalised using the method of [20] as implemented in the edgeR R/Bioconductor package [23].

Statistics of RNA-seq mapping and distribution of reads for pre-mRNA and mRNA transcripts are presented in Tables S2 and S3 as well as Fig. S9.

C Filtering of active genes

We removed genes with no clear time-dependent activity by fitting time-dependent Gaussian process models to the activity curves and only keeping genes with Bayes factor at least 3 in favour of the time-dependent model compared to a null model with no time dependence. We also removed genes that had no pol-II observations at 2 or more time points. This left 4420 genes for which we fitted the models.

D Pol II ChIP-seq data processing

The ChIP-seq data were processed into time series by summarising the pol-II occupancy over time for each human gene (Ensembl version 68 annotation was used for gene positions), by a series of steps as follows.

1. Each gene was divided into 200 bp bins and levels of pol-II activity were computed at each time point as the total weighted count of reads overlapping each bin, where each read was weighted by how many basepairs in the read overlap the bin, as follows. Only uniquely mapped reads were used. For any read that at least partially overlaps a bin, the number of basepairs overlapping the bin was added into the activity level of the bin. For any read spanning multiple bins, the number of basepairs overlapping each bin were added into activity of that bin. The Genomatix mapping software provides alignment scores (values between 0 and 1; with our threshold only between 0.92 and 1) for mapping reads to the genome; for any read having alignment score less than 1, the number of overlapping basepairs added to each bin was multiplied by the alignment score.
2. A noise removal was then done: a noise level was computed as the average activity level in 74 manually selected regions from Chromosome 1 that were visually determined to be inactive over the measurement time points, as follows. The regions were divided into 200 bp bins, and total weighted counts of reads overlapping each bin (each read weighted by the number of basepairs overlapping the bin) were computed in the same way as for the genes in the previous step. For each time point, the noise level was computed as the average activity level over all bins from all 74 regions. The computed noise level was subtracted from the mean of each bin in each gene, thresholding the result at zero. A list of the empty regions used is included as a Supplementary Dataset S1.
3. As the number of ChIP-seq reads collected overall for pol-II varies between time points, a robust normalisation was done. After the previous noise removal step, for each gene g at each time t we compute the mean of the remaining activity (activity level after noise removal) over bins of the gene, denoted as r_{gt} . The activity levels are weighted counts of basepairs from reads overlapping the gene; we select genes having sufficient activity, that is, at least $5 \cdot 200$ overlapping basepairs from reads over each 200 bp bin of the gene, on average over the bins. For each gene g let $T_g = \{t' \in \{5, 10, \dots, 1280 \text{ min}\} | r_{gt'} > 5 \cdot 200\}$ denote those time points (except the first time point) where the gene has sufficient activity. For each time point we compute a normalisation factor of [20]

$$C_t = \text{Median}_g \left\{ \frac{r_{gt}}{\text{GeomMean}_{t'}\{r_{gt'}\}} \right\} .$$

where $\text{Median}_g\{\cdot\}$ denotes median over genes and $\text{GeomMean}_{t'}\{r_{gt'}\} = (\prod_{t' \in T_g} r_{gt'})^{1/|T_g|}$ is the geometric mean over the

time points having sufficient activity for gene g . The median is computed for time points after the first time point; for the first time point $t = 0$ min we set $C_t = 1$. The factor C_t normalises all the gene activity levels (weighted read counts) at a time point downwards if genes at that time point have unusually many reads, exceeding their (geometric) mean activity level, and normalises upwards if gene activity levels fall under their mean activity level.

4. Lastly, time series summaries were computed for pol-II at each gene. For each gene at each time point t , the mean activity level (weighted read-count) of pol-II over bins in the 20% section of the gene nearest to transcription end was computed, normalised by C_t . This measured pol-II level represents transcriptional activity that had successfully passed through the gene to the transcription end site; it is expected to correspond better with mRNA production rate than pol-II activity at the transcription start of the gene, since pol-II near the transcription start site can be in the active or inactive state and after activation may require a significant time for transcription to complete.
5. For a small number of genes where the active mRNA transcripts covered only part of the gene, we considered the area from the first active exon to last active exon, and summarised the gene using the 20% section nearest to the end of the area. Active transcripts were defined here as transcripts with a mean of more than 1.1 assigned counts in the BitSeq posterior expression estimates. BitSeq uses a prior that assigns 1 “pseudo-count” per transcript, so the active transcripts were only required to have minimal posterior expression that was distinguishable from the prior. A list of active transcripts is included as Supplementary Dataset S2.
6. Lastly, for mathematical convenience, for each pol-II time series we subtracted from all time points the minimum value over the time points.

E Differential equation based modelling

We model the role of pol-II as a catalyst of the transcription of DNA into mRNA as a differential equation for each gene; the differential equation relates the pol-II time series $p(t)$ of the gene and the corresponding mRNA time series $m(t)$.

Let us assume the momentary pol-II activity directly represents the momentary rate of transcription, potentially with a delay, and that the mRNA decays at a constant rate. We model this as a linear differential equation

$$\frac{dm(t)}{dt} = \beta_0 + \beta p(t - \Delta) - \alpha m(t) \quad (\text{S2})$$

where Δ is a delay parameter between the pol-II activity and the momentary transcription rate, β_0 is a parameter representing the *baseline transcription rate*

from unobservable pol-II background (baseline production level of mRNA), β is a parameter representing *transcriptional efficiency*, that is, sensitivity of the transcription rate to activity of pol-II, and α is a constant mRNA *decay* rate parameter that is related to mRNA half-life $t_{1/2}$ through $\alpha = \ln(2)/t_{1/2}$.

The momentary mRNA level $m(t)$ can be solved from the differential equation to yield the following solution:

$$m(t) = m_0 e^{\alpha(t_0-t)} + \frac{\beta_0}{\alpha} (1 - e^{-\alpha t}) + \beta e^{-\alpha t} \int_{u=0 \text{ min}}^t e^{\alpha u} p(u - \Delta) du \quad (\text{S3})$$

where pol-II activity is assumed to start at $t = 0 \text{ min}$ ($p(t) = 0$ for $t < 0 \text{ min}$), $t_0 \gg 0 \text{ min}$ is the time of the first observation, and m_0 is an initial mRNA abundance at t_0 which is inferred as a parameter of the model. No parametric assumptions are made about the shape of the pol-II time series function $p(t)$, and the only assumption about the mRNA level $m(t)$ is that it arises through the differential equation.

The linear differential equation (S2) and its linear solution operator (S3) are similar to those used previously in [9–11] except for the added delay. As in the previous works, the linearity of the solution operator permits exact joint Gaussian process (GP) modelling over $p(t)$ and $m(t)$.

F Gaussian process inference

We model pol-II and mRNA time series, $p(t)$ and $m(t)$, in a nonparametric fashion which avoids the assumption of a specific parametric shape for the time series function; instead, we set a GP prior over the time series functions.

For each gene, GP inference of the posterior distribution over the underlying pol-II and mRNA time series can be done in closed form given fixed values of the differential equation parameters. GP inference is based on mean and covariance functions. Below we describe the GP model of pol-II and mRNA, their respective mean functions and covariance functions, and the cross-covariance function between pol-II and mRNA. GP inference of the posterior is then a standard inference equation which we provide for completeness.

The above inference provides a posterior distribution over the profiles $p(t)$ and $m(t)$ given known values for the differential equation parameters. However, these values are not known and to infer a full posterior over both time series and these parameters we carry out Markov Chain Monte Carlo (MCMC) sampling over the parameter values, as described in Section “Parameter inference by Hamiltonian Monte Carlo sampling”.

F.1 GP model of pol-II

For each gene, we model the pol-II activity time series in a nonparametric fashion by applying a GP prior over the shapes of the time series. Previous similar GP models [9–11] have used a squared exponential covariance function for $p(t)$, as that allows derivation of all the shared covariances in closed form.

This covariance has the limitation that it is stationary, and functions following it revert to zero away from data. These properties severely degrade its performance on our highly unevenly sampled data. To avoid this, we model $p(t)$ as an *integral* of a function having a GP prior with a squared exponential covariance: then the posterior mean of $p(t)$ tends to remain constant between observed data. That is, we model

$$p(t) = p_0 + \int_{u=0}^t v(t)dt \quad (\text{S4})$$

where p_0 is the initial value at time $t = 0$ min, and assign a GP prior with the squared exponential covariance over $v(t)$; as a result $p(t)$ will also have a GP prior whose covariance function is an integral of the covariance function of $v(t)$. For mathematical convenience we assume $p(t) = 0$ min for $t < 0$ min, and set the initial observation time t_0 to a sufficiently large value to avoid any discontinuity resulting from assumption in pol-II or mRNA modeling.

To define the GP prior, we first define the mean function of $p(t)$. Assume that $v(t)$ is drawn from a zero-mean GP prior with a squared exponential covariance function $k_v(t, t') = C_p \cdot \exp(-(t - t')^2/l^2)$ where C_p is a magnitude parameter and l is a length scale, which has been parametrised in a non-standard manner to simplify the derivations. Then $E[p(t)] = E[p_0] + \int_{u=t_0}^t E[v(t)]dt = E[p_0] \equiv \mu_p$ for $t \geq 0$ min.

Next we compute the corresponding covariance function for the GP prior of $p(t)$. We have

$$\begin{aligned} k_p(t, t') &\equiv E[(p(t) - \mu_p)(p(t') - \mu_p)] = \int_{s=0}^t \int_{s'=0}^{t'} k_v(s, s')dsds' \\ &= \frac{\sqrt{\pi}C_p l}{2} \int_{s=0}^t \left(\text{erf}((t' - s)/l) - \text{erf}(-s/l) \right) ds \quad (\text{S5}) \end{aligned}$$

The remaining integral over the erf functions can be computed using integration by parts. After straightforward manipulation, the integral becomes

$$\begin{aligned} k_p(t, t') &= \frac{C_p \sqrt{\pi} l^2}{2} \left(t_l \text{erf}(t_l) + t'_l \text{erf}(t'_l) - (t'_l - t_l) \text{erf}(t'_l - t_l) \right) \\ &\quad + \frac{C_p l^2}{2} \left(\exp(-t_l^2) + \exp(-(t'_l)^2) - \exp(-(t'_l - t_l)^2) - 1 \right). \quad (\text{S6}) \end{aligned}$$

where we denoted $t_l = t/l$ and $t'_l = t'/l$ for brevity.

The right-hand side is the covariance function $k_p(t, t')$ of the integrated squared-exponential GP prior for pol-II.

F.2 GP model of mRNA

We model the mRNA abundance in a similar nonparametric fashion as the pol-II activity. Since the mRNA is related to pol-II through a differential equation, the GP prior of mRNA can be computed from the GP prior of pol-II through the

differential equation. In particular, as shown in Eq. (S3), the mRNA time series is an integral of the pol-II time series. Since integration is a linear operation, the expected mRNA time series is an integral of the expected pol-II time series; that is, the GP mean function of mRNA is an integral of the mean function of pol-II, so that

$$\begin{aligned}
\mu_m(t) &\equiv E[m(t)] = m_0 e^{\alpha(t_0-t)} + \\
&\quad \frac{\beta_0}{\alpha} (1 - e^{-\alpha t}) + \beta e^{-\alpha t} \int_{u=0}^t e^{\alpha u} E[p(u - \Delta)] du \\
&= m_0 e^{-\alpha(t-t_0)} + \frac{\beta_0}{\alpha} (1 - e^{-\alpha t}) + \beta e^{-\alpha t} \int_{u=\Delta}^t e^{\alpha u} \mu_p du \\
&= m_0 e^{-\alpha(t-t_0)} + \frac{\beta_0}{\alpha} (1 - e^{-\alpha t}) + \frac{\beta \mu_p}{\alpha} (1 - e^{-\alpha(t-\Delta)}) \quad (S7)
\end{aligned}$$

where the third line follows since pol-II activity starts at $t = 0$ min. Note that the start of pol-II activity at $t = 0$ min is for mathematical convenience, and the initial observation time t_0 will be set to a sufficiently large value so that the $t - \Delta \geq 0$ min for all $t \geq t_0$ and hence observed mRNA values are integrated over active pol-II only regardless of delay Δ .

We next compute the corresponding covariance function for the GP prior of mRNA. The covariance function arises from computing the integral relating mRNA to pol-II as follows:

$$\begin{aligned}
k_m(t, t') &\equiv E[(m(t) - \mu_m(t))(m(t') - \mu_m(t'))] \\
&= E \left[\left(\beta e^{-\alpha t} \int_{u=0}^t e^{\alpha u} p(u - \Delta) du - \frac{\beta \mu_p}{\alpha} (1 - e^{-\alpha(t-\Delta)}) \right) \right. \\
&\quad \left. \left(\beta e^{-\alpha t'} \int_{u'=0}^{t'} e^{\alpha u'} p(u' - \Delta) du' - \frac{\beta \mu_p}{\alpha} (1 - e^{-\alpha(t'-\Delta)}) \right) \right] \\
&= \beta^2 E \left[\left(e^{-\alpha t} \int_{u=\Delta}^t e^{\alpha u} p(u - \Delta) du - \frac{\mu_p}{\alpha} (1 - e^{-\alpha(t-\Delta)}) \right) \right. \\
&\quad \left. \left(e^{-\alpha t'} \int_{u'=\Delta}^{t'} e^{\alpha u'} p(u' - \Delta) du' - \frac{\mu_p}{\alpha} (1 - e^{-\alpha(t'-\Delta)}) \right) \right] \quad (S8)
\end{aligned}$$

where the last equality follows since pol-II activity starts at time 0 min. The computation of the integrals follows similar steps as computation of the pol-II GP covariance. The result is

$$k_m(t, t') = k_{m,1}(t, t') + k_{m,2}(t, t') + k_{m,3}(t, t') + k_{m,4}(t, t') \quad (S9)$$

where we divided the covariance function into four parts. The first part is

$$\begin{aligned}
k_{m,1}(t, t') &= \frac{\sqrt{\pi} l C_p \beta^2}{2\alpha^2} \left(\left(t_\Delta - \frac{1}{\alpha} + \frac{\exp(-\alpha t'_\Delta)}{\alpha} \right) \operatorname{erf} \left(\frac{t_\Delta}{l} \right) \right. \\
&\quad \left. + \left(t'_\Delta - \frac{1}{\alpha} + \frac{\exp(-\alpha t_\Delta)}{\alpha} \right) \operatorname{erf} \left(\frac{t'_\Delta}{l} \right) - (t_\Delta - t'_\Delta) \operatorname{erf} \left(\frac{t_\Delta - t'_\Delta}{l} \right) \right) \quad (S10)
\end{aligned}$$

where $t_\Delta = \max(0, \min(t, t - \Delta))$. The second part is

$$k_{m,2}(t, t') = \frac{l^2 C_p \beta^2}{2\alpha^2} \left(\exp\left(-\left(\frac{t_\Delta}{l}\right)^2\right) + \exp\left(-\left(\frac{t'_\Delta}{l}\right)^2\right) - \exp\left(-\left(\frac{t_\Delta - t'_\Delta}{l}\right)^2\right) - 1 \right). \quad (\text{S11})$$

The third part is

$$k_{m,3}(t, t') = -\sqrt{\pi} l C_p \beta^2 \left(\frac{\alpha^{-3}}{4} \exp(\alpha^2 l^2 / 4 + \alpha(t_\Delta - t'_\Delta)) (\text{erf}(\alpha l / 2 + t_\Delta / l) - \text{erf}(\alpha l / 2 + (t_\Delta - t'_\Delta) / l)) + \frac{\alpha^{-3}}{4} \exp(\alpha^2 l^2 / 4 - \alpha t'_\Delta - \alpha t_\Delta) (\text{erf}(\alpha l / 2) - \text{erf}(\alpha l / 2 - t'_\Delta / l)) - \frac{\alpha^{-3}}{2} \exp(\alpha^2 l^2 / 4 - \alpha t'_\Delta) (\text{erf}(\alpha l / 2) - \text{erf}(\alpha l / 2 - t'_\Delta / l)) \right). \quad (\text{S12})$$

The fourth part is

$$k_{m,4}(t, t') = -\sqrt{\pi} l C_p \beta^2 \left(\frac{\alpha^{-3}}{4} \exp(\alpha^2 l^2 / 4 - \alpha(t_\Delta - t'_\Delta)) (\text{erf}(\alpha l / 2 + t'_\Delta / l) - \text{erf}(\alpha l / 2 - (t_\Delta - t'_\Delta) / l)) + \frac{\alpha^{-3}}{4} \exp(\alpha^2 l^2 / 4 - \alpha t_\Delta - \alpha t'_\Delta) (\text{erf}(\alpha l / 2) - \text{erf}(\alpha l / 2 - t_\Delta / l)) - \frac{\alpha^{-3}}{2} \exp(\alpha^2 l^2 / 4 - \alpha t_\Delta) (\text{erf}(\alpha l / 2) - \text{erf}(\alpha l / 2 - t_\Delta / l)) \right). \quad (\text{S13})$$

F.3 GP joint model

To define the full GP prior over both pol-II and mRNA, it remains to define the cross-covariance function between pol-II and mRNA. The full GP covariance is defined by the individual covariances of pol-II and mRNA and the cross-covariance.

The cross-covariance function between (noiseless) mRNA abundance $m(t)$ at time t and (noiseless) pol-II activity $p(t')$ at time t' is computed with similar steps as the computation of the mRNA covariance function. The result is

$$k_{mp}(t, t') = E[(m(t) - \mu_m(t))(p(t') - \mu_p(t'))] = k_{mp,1}(t, t') + k_{mp,2}(t, t') + k_{mp,3}(t, t') \quad (\text{S14})$$

where for convenience we separated the kernel function into a sum of three

components. The first component part of the kernel can be written as

$$\begin{aligned}
k_{mp,1}(t, t') = & \\
& - \frac{\sqrt{\pi}\beta^2\sqrt{C_p}l}{2\alpha^2} \exp\left(\left(\frac{\alpha l}{2}\right)^2 - \alpha t_\Delta + \alpha t'\right) \\
& \cdot \left[\operatorname{erf}\left(\frac{\alpha l}{2} + \frac{t'}{l}\right) - \operatorname{erf}\left(\frac{\alpha l}{2} + \frac{t' - t_\Delta}{l}\right) \right] \\
& - \frac{\sqrt{\pi}\beta^2\sqrt{C_p}l}{2\alpha^2} \exp\left(\left(\frac{\alpha l}{2}\right)^2 - \alpha t_\Delta\right) \\
& \cdot \left[\operatorname{erf}\left(\frac{\alpha l}{2} - \frac{t_\Delta}{l}\right) - \operatorname{erf}\left(\frac{\alpha l}{2}\right) \right]. \quad (\text{S15})
\end{aligned}$$

The second component can be written as

$$\begin{aligned}
k_{mp,2}(t, t') = & \\
& - \frac{\beta^2\sqrt{C_p}l^2}{2\alpha} \left[\exp\left(-\left(\frac{t_\Delta - t'}{l}\right)^2\right) - \exp\left(-\left(\frac{t_\Delta}{l}\right)^2\right) \right. \\
& \left. + 1 - \exp\left(-\left(\frac{t'}{l}\right)^2\right) \right]. \quad (\text{S16})
\end{aligned}$$

The third component can be written as

$$\begin{aligned}
k_{mp,3}(t, t') = & - \frac{\sqrt{\pi}\beta^2\sqrt{C_p}l}{2\alpha} \left[(t_\Delta - t' - 1/\alpha)\operatorname{erf}((t_\Delta - t')/l) \right. \\
& \left. - (t_\Delta - 1/\alpha)\operatorname{erf}(t_\Delta/l) - (t' + \exp(-\alpha t_\Delta)/\alpha)\operatorname{erf}(t'/l) \right]. \quad (\text{S17})
\end{aligned}$$

F.4 Observation model

In order to fit the models of the pol-II and mRNA functions to observations, we need an observation model. It is assumed that we observe noisy values $\tilde{m}(t) = m(t) + e_m(t)$ and $\tilde{p}(t) = p(t) + e_p(t)$ where $e_m(t)$ and $e_p(t)$ are zero-mean Gaussian noise independently sampled for each time point. For simplicity we assume the noise variance of $e_p(t)$ is a constant σ_p^2 and infer it as a parameter of the model. We estimate the mRNA noise variances $\sigma_m^2(t)$ for each time point t as sums of a shared constant σ_m^2 and a fixed variance inferred by BitSeq by combining the technical quantification uncertainty from BitSeq expression estimation with an estimate of biological variance from the BitSeq differential expression model (full details are in Sec. RNA-seq data processing).

Since the noise is zero-mean, the GP prior for the noisy observations has the same means as the noiseless means, that is, $E[\tilde{m}(t)] = E[m(t)]$ and $E[\tilde{p}(t)] = E[p(t)]$. Since the noise is independently added to each observation, the covariance function of observed pol-II becomes

$$k_{\tilde{p}}(t, t') = k_p(t, t') + \delta(t, t')\sigma_p^2 \quad (\text{S18})$$

where $\delta(t, t') = 1$ if $t = t'$ and zero otherwise, the covariance function of observed mRNA becomes

$$k_{\tilde{m}}(t, t') = k_m(t, t') + \delta(t, t')\sigma_m^2(t), \quad (\text{S19})$$

and the cross-covariance function between observed pol-II and mRNA is the same as the noiseless version so that

$$k_{\tilde{m}\tilde{p}}(t, t') = k_{mp}(t, t'). \quad (\text{S20})$$

The GP prior over time series functions and the observation model together define a full probability model for the pol-II and mRNA data. As the observations are noisy and available only at a small set of time points, we will apply Bayesian inference to infer the underlying time series $m(t)$ and $p(t)$ from the observations.

F.5 Covariance matrix for GP inference

Given a set of time points, here the 10 time points

$$\begin{aligned} T_{obs} &= t_0 + (0, 5, 10, 20, 40, 80, 160, 320, 640, 1280) \\ &= (t_1, \dots, t_N) \end{aligned}$$

where t_0 is the initial observation time and the numbers denote time in minutes, and the corresponding observation data consisting of $N = 10$ pol-II observations and $N = 10$ mRNA observations $\mathcal{D} = (\tilde{p}(t_1), \dots, \tilde{p}(t_N), \tilde{m}(t_1), \dots, \tilde{m}(t_N))$, we wish to compute the posterior distribution of GP hyperparameters, and to predict the shape of the underlying time series functions $p(t)$ and $m(t)$ given the posterior. We will especially wish to study delay between pol-II and mRNA; for mathematical convenience we set $t_0 = 300$ min and consider mRNA delay parameters $0 \leq \Delta \leq 300$ min.

For GP inference, given the hyperparameters we must compute the prior GP covariance matrix for the observations \mathcal{D} . We describe the matrix here in a general form which is needed later for inference of time series values at previously unseen time points.

The covariance matrix describes covariance between measurements at one set of time points (indexed by rows of the matrix) and another set of time points (indexed by columns of the matrix). Let $T_{row} = (t_{row,1}, \dots, t_{row,N_{row}})$ be a vector of N_{row} time indices for rows of the matrix, and let $T_{col} = (t_{col,1}, \dots, t_{col,N_{col}})$ be the vector of N_{row} time indices for columns of the matrix.

The resulting covariance matrix $K(T_{row}, T_{col})$ has the block structure

$$K(T_{row}, T_{col}) = \begin{bmatrix} K_{\tilde{p}} & K_{\tilde{p}\tilde{m}} \\ K_{\tilde{m}\tilde{p}} & K_{\tilde{m}} \end{bmatrix} \quad (\text{S21})$$

where each block is a $N_{row} \times N_{col}$ matrix of covariance function values between the time points $t \in T_{row}$ and the time points $t' \in T_{col}$, so that $K_{\tilde{p}}$ is composed of values $k_{\tilde{p}}(t, t')$, $K_{\tilde{m}}$ is composed of values $k_{\tilde{m}}(t, t')$, $K_{\tilde{m}\tilde{p}}$ is composed of the cross-covariance values $k_{\tilde{m}\tilde{p}}(t, t')$, and $K_{\tilde{p}\tilde{m}}$ is composed of the cross-covariance values $k_{\tilde{p}\tilde{m}}(t', t)$. The covariance matrix of observed data is then simply $K_{obs} = K(T_{obs}, T_{obs})$.

F.6 Marginal likelihood function

The analytical tractability of the GP model allows us to marginalise out the latent functions $p(t)$ and $m(t)$ to compute a marginal likelihood that only depends on the model parameters. The marginal probability density of the observations \mathcal{D} is Gaussian and the marginal log-likelihood is

$$\log P(\mathcal{D}) = (1/2)(-d \log(2\pi) - \log(|K_{obs}|) - u^\top K_{obs}^{-1} u) \quad (\text{S22})$$

where P denotes the marginal probability density, $d = 20$ is the total number of pol-II and mRNA observations and u is the column vector of observations with their expected values subtracted, $u = [\tilde{p}(t_1) - E[\tilde{p}(t_1)], \dots, \tilde{p}(t_N) - E[\tilde{p}(t_N)], \tilde{m}(t_1) - E[\tilde{m}(t_1)], \dots, \tilde{m}(t_N) - E[\tilde{m}(t_N)]]^\top$.

F.7 Posterior prediction

The analytical tractability of the GP model also allows us to obtain the full posterior distribution over the latent functions in closed form given the parameters. Given the observed data, we can thus compute the mean and covariance of the underlying time series function values at each time point, as expectations over the posterior distribution of the underlying functions. For N^* new time points $T^* = (t_1^*, \dots, t_{N^*}^*)$ the posterior mean is

$$E[[\tilde{p}(t_1^*), \dots, \tilde{p}(t_{N^*}^*), \tilde{m}(t_1^*), \dots, \tilde{m}(t_{N^*}^*)] | \mathcal{D}] = u_{\text{prior}}^* + K(T^*, T_{obs}) K_{obs}^{-1} u \quad (\text{S23})$$

where

$$u_{\text{prior}}^* = [E[\tilde{p}(t_1^*)], \dots, E[\tilde{p}(t_{N^*}^*)], E[\tilde{m}(t_1^*)], \dots, E[\tilde{m}(t_{N^*}^*)]]^\top \quad (\text{S24})$$

is the vector of prior means computed at the new time points, and the posterior covariance matrix is

$$\begin{aligned} Cov([\tilde{p}(t_1^*), \dots, \tilde{p}(t_{N^*}^*), \tilde{m}(t_1^*), \dots, \tilde{m}(t_{N^*}^*)] | \mathcal{D}) \\ = K(T^*, T^*) - K(T^*, T_{obs}) K_{obs}^{-1} K(T^*, T_{obs})^\top. \end{aligned} \quad (\text{S25})$$

The log-likelihood and predictions of function values described here are computed given fixed values of hyperparameters of the GP prior and the observation model. We will compute a posterior distribution for the hyperparameters, given suitable prior distributions for each. This will allow summarisation of underlying pol-II and mRNA functions and GP parameters over the posterior distribution of the hyperparameters. We next describe the prior distributions of hyperparameters and then describe the sampling based inference of hyperparameter posterior distributions.

F.8 Parameter prior distributions

All parameters except the delay Δ have approximately uniform bounded logistic-normal priors. These priors were used because of convenience: they allow easy

Hamiltonian Monte Carlo sampling that requires very little tuning (see below for details).

The density of the logistic-normal prior $\text{logit-normal}(\mu, \sigma^2, a, b)$ with location parameter μ and scale parameter σ^2 for variable θ bounded to the interval $[a, b]$ is

$$p(\theta|\mu, \sigma^2, a, b) = \frac{1}{\sqrt{2\pi\sigma^2}} \exp\left(-\frac{(\text{logit}((\theta - a)/(b - a)) - \mu)^2}{2\sigma^2}\right) \cdot \frac{b - a}{(\theta - a)(b - \theta)}, \quad (\text{S26})$$

where $\text{logit}(x) = \log(x/(1 - x))$. We use $\mu = 0$ and $\sigma = 2$ which lead to an approximately uniform distribution on the interval $[a, b]$. The interval bounds a, b for all variables are presented in Table S1.

For the delay Δ we use a prior with $\mu = -2, \sigma = 2$ to reflect our prior belief that the delays should in most cases be small. For β and l we set the priors with respect to β^2 and $2/l^2$ respectively, because these are more convenient as model parameters.

Parameter	Lower bound a	Upper bound b
$2/l^2$	$(1280 \text{ min})^{-2}$ $\approx 6.1 \cdot 10^{-7} \text{ min}^{-2}$	$(5 \text{ min})^{-2}$ $= 4 \cdot 10^{-2} \text{ min}^{-2}$
C_p	$2 \cdot 10^{-4} \hat{\sigma}_{Pol2}^2$	$\hat{\sigma}_{Pol2}^2$
σ_p^2	$0.05 \hat{\sigma}_{Pol2}^2$	$\hat{\sigma}_{Pol2}^2$
α	$1 \cdot 10^{-6} \text{ min}^{-1}$	$\log(2) \text{ min}^{-1} \approx 0.69 \text{ min}^{-1}$
β^2	$1 \cdot 10^{-6} \text{ min}^{-2}$	1 min^{-2}
Δ	0 min	299 min
β_0	0 min^{-1}	1 min^{-1}
m_0	0	2
μ_p	0	1

Table S1: Bounds for bounded logistic-normal priors of differential equation parameters in the GP inference of pol-II and mRNA time series. Each parameter is bounded to an interval $[a, b]$, we list the values of the lower bound a and upper bound b . Here $\hat{\sigma}_{Pol2}^2$ is the empirical variance of the pol-II time series after preprocessing.

F.9 Parameter inference by Hamiltonian Monte Carlo sampling

Given the data and the priors for the parameters, we apply fully Bayesian inference with Hamiltonian Monte Carlo (HMC) sampling [15] to obtain samples from the posterior distribution of the parameters. HMC is a MCMC algorithm that uses gradients of the target distribution to simulate a Hamiltonian dynamical system with an energy function based on the target distribution. This allows taking long steps while maintaining a high acceptance rate in the sampling.

In order to apply HMC more easily, we transform all parameters to an unbounded space using the logistic transformation. The logistic-normal priors correspond to normal priors on the transformed variables, which effectively prevent the sampler from wandering off to the saturated region of the transformation near the bounds of the intervals.

We run 4 parallel chains starting from different random initial states to allow convergence checking. We use the HMC implementation from NETLAB toolkit in Matlab with momentum persistence and number of leap frog steps $\tau = 20$ which were found to work well in all cases. The step length ϵ is tuned separately for every model (see below). After tuning, each chain is run for 10000 iterations. The samples are then thinned by a factor of 10, and the first half of the samples are discarded, leaving 500 samples from each chain, 2000 in all. Convergence is monitored using the potential scale reduction factor $\sqrt{\hat{R}}$ [21]. $\sqrt{\hat{R}}$ is computed separately for each variable, and if any of them is greater than 1.2, the result is discarded and a new sample obtained in a similar manner. The 9 genes that did not converge after 10 iterations of this process were removed from further analysis. In most cases these had severely multimodal delay distributions that were difficult to sample from and would have made further analysis difficult.

F.9.1 Tuning

The applied logistic transformation and priors together allow using the same global step length ϵ for all variables, or using the identity matrix as the mass matrix in the HMC formulation. The step length ϵ was determined by trying different alternatives in the set $\{10^{-5}, 10^{-4}, 10^{-3}, 0.003, 0.005, 0.01, 0.03, 0.05, 0.07, 0.1, 0.3, 0.5, 1\}$ in increasing order, running the sampler for 100 steps and using the largest value with at least 80% acceptance rate. This target rate is higher than usual in random walk MCMC because HMC acceptance rate should be nearly 100% even with very long steps if the Hamiltonian system is simulated accurately.

F.9.2 Summarisation of inference results

The inference results are summarised using the median of the posterior samples. This is a convenient statistic because it is invariant to transformations of the parameter space, such as those used during the sampling.

F.10 Validation of the GP modelling results

In order to validate the GP model, we implemented inference for the same ODE using a smoothing spline fit for pol-II. A comparison of the results for the subset of genes that yielded reliable results with the spline approach is presented in Fig. S10.

G Filtering of results

Reliable posterior samples were obtained for models of 4373 genes. 4304 of these had multiple-exon transcripts, and could thus be used for intron analyses. These genes were further filtered to remove bad fits by only keeping genes that satisfy the following:

1. The global maximum t_{\max} of $p(t)$ posterior mean $\bar{p}(t)$ in the interval $t \in [0 \text{ min}, 1280 \text{ min}]$ occurs in the interval $t_{\max} \in (1 \text{ min}, 160 \text{ min})$. This condition ensures the profile has a peak in the densely sampled region which is necessary for accurate estimation of the delay.
2. The posterior median delay $\hat{\Delta} < 120 \text{ min}$. Because of the increasingly sparse sampling, longer delay estimates were considered unreliable. The specific cut-off was determined by visual inspection of the fits to rule out implausible ones.
3. The posterior mean $\bar{p}(t)$ of $p(t)$ does not change too much just before $t = 0 \text{ min}$. This condition is necessary to avoid cases where a long delay pushes distinctive features of $m(t)$ to $p(t), t < 0 \text{ min}$, which conflicts with the assumption that the system is at a steady state until $t = 0 \text{ min}$. Quantitatively, we define an index

$$D = D_- - D_+ = D_{[-30 \text{ min}, 0 \text{ min}]} - D_{[0 \text{ min}, 10 \text{ min}]} \quad (\text{S27})$$

where

$$D_I = \left(\max_{t \in I} [\bar{p}(t)] - \min_{t \in I} [\bar{p}(t)] \right) / \max_{t \in [-30 \text{ min}, 1280 \text{ min}]} [\bar{p}(t)], \quad (\text{S28})$$

and only include genes with

$$D < 0.05. \quad (\text{S29})$$

Intuitively, D_I looks at the magnitude of change in $\bar{p}(t)$ in the interval I relative to the global magnitude of change in $\bar{p}(t)$. The final statistic D looks for genes that have small changes in $[-30 \text{ min}, 0 \text{ min}]$, but forgives genes with early large changes in $[0 \text{ min}, 10 \text{ min}]$ because these would often spill over to $t < 0 \text{ min}$ because of the properties of the GP model. The cut-off 0.05 represents 5% change in magnitude, which seems reasonably small. The main conclusions of the work are robust to different cutoffs, as demonstrated in Fig. S5 below.

After these filtering steps, there were 1814 genes left for the analysis.

Main results under an additional filter of setting a maximum for posterior inter-quartile range are presented in Fig. S11.

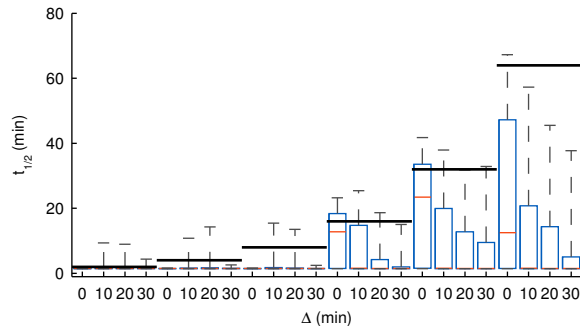


Figure S1: Boxplots of parameter posterior distributions illustrating parameter estimation performance on synthetic data for the mRNA half life $t_{1/2} = \log(2)/\alpha$. The strong black lines indicate the ground truth used in data generation. The box extends from 25th to 75th percentile of the posterior distribution while the whiskers extend from 9th to 91st percentile. The model often underestimates the half lives, especially in the presence of a significant delay.

H Synthetic data generation

The synthetic data were generated by fitting a GP with the MLP covariance [24] to the Pol-II measurements of the gene TIPARP (ENSG00000163659), and numerically solving the mRNA level using Eq. (S3) with the GP posterior mean as $p(t)$. The parameters used were: $\Delta \in \{0, 10, 20, 30\}$ min, $t_{1/2} = \log(2)/\alpha \in \{2, 4, 8, 16, 32, 64\}$ min, $\beta_0 = 0.005$, $\beta = 0.03$, $m_0 = 0.008/\alpha$. The parameter values were chosen empirically to get profiles that approximately fitted the actual mRNA observations while looking reasonable and informative across the entire range of parameter values.

I Supplementary Results

In this section we provide supplementary Figs. S1–S8 discussed in the main paper as well as Figs. S9–S11 discussed in the Supplementary Methods.

I.1 Estimation of delays under changing mRNA half life

References

- [1] S. Hao and D. Baltimore. RNA splicing regulates the temporal order of TNF-induced gene expression. *Proc Natl Acad Sci U S A*, 110(29):11934–11939, Jul 2013.
- [2] N. A. M. Monk. Oscillatory expression of Hes1, p53, and NF-kappaB driven by transcriptional time delays. *Curr Biol*, 13(16):1409–1413, Aug 2003.

Table S2: Fraction of reads mapping to mRNA transcripts alone (junction reads), pre-mRNA transcripts alone and both across all time points.

t	mRNA	pre-mRNA	both
0 min	0.035	0.287	0.678
5 min	0.033	0.308	0.659
10 min	0.036	0.270	0.694
20 min	0.033	0.321	0.647
40 min	0.033	0.312	0.654
80 min	0.031	0.372	0.597
160 min	0.033	0.331	0.636
320 min	0.033	0.327	0.640
640 min	0.034	0.330	0.636
1280 min	0.032	0.339	0.629

- [3] A. Zaslaver, A. E. Mayo, R. Rosenberg, P. Bashkin, H. Sberro, M. Tsalyuk, M. G. Surette, and U. Alon. Just-in-time transcription program in metabolic pathways. *Nat Genet*, 36(5):486–491, May 2004.
- [4] A. Zeisel, W. J. Kstler, N. Molotski, J. M. Tsai, R. Krauthgamer, J. Jacob-Hirsch, G. Rechavi, Y. Soen, S. Jung, Y. Yarden, and E. Domany. Coupled pre-mRNA and mRNA dynamics unveil operational strategies underlying transcriptional responses to stimuli. *Mol Syst Biol*, 7:529, 2011.
- [5] Y. L. Khodor, J. S. Menet, M. Tolan, and M. Rosbash. Cotranscriptional splicing efficiency differs dramatically between *Drosophila* and mouse. *RNA*, 18(12):2174–2186, 2012.
- [6] A. Pandya-Jones, D. M. Bhatt, C.-H. Lin, A.-J. Tong, S. T. Smale, and D. L. Black. Splicing kinetics and transcript release from the chromatin compartment limit the rate of Lipid A-induced gene expression. *RNA*, 19(6):811–827, Jun 2013.
- [7] M. Rabani, J. Z. Levin, L. Fan, X. Adiconis, R. Raychowdhury, M. Garber, A. Gnirke, C. Nusbaum, N. Hacohen, N. Friedman, I. Amit, and A. Regev. Metabolic labeling of RNA uncovers principles of RNA production and degradation dynamics in mammalian cells. *Nat Biotechnol*, 29(5):436–442, May 2011.
- [8] G. L. Martelot, D. Canella, L. Symul, E. Migliavacca, F. Gilardi, R. Liechti, O. Martin, K. Harshman, M. Delorenzi, B. Desvergne, W. Herr, B. Deplancke, U. Schibler, J. Rougemont, N. Guex, N. Hernandez, F. Naef, and C. Consortium. Genome-wide RNA polymerase II profiles and RNA accumulation reveal kinetics of transcription and associated epigenetic changes during diurnal cycles. *PLoS Biol*, 10(11):e1001442, Nov 2012.
- [9] N. D. Lawrence, G. Sanguinetti, and M. Rattray. Modelling transcriptional regulation using Gaussian processes. In B. Schölkopf, J. C. Platt, and

Table S3: Fraction of reads assigned by BitSeq on average to mRNA transcripts and pre-mRNA transcripts, as well as fraction predicted for pre-mRNA when distributing 'both' category reads from Table S2 uniformly according to average transcript lengths. Only multi-exon genes are considered here, because the division is not meaningful for others. The results demonstrate that BitSeq can split the RNA-seq data to mRNA and pre-mRNA fractions in a meaningful manner.

t	mRNA	pre-mRNA	pre-mRNA pred.
0 min	0.62	0.38	0.37
5 min	0.59	0.41	0.39
10 min	0.64	0.36	0.36
20 min	0.58	0.42	0.40
40 min	0.59	0.41	0.40
80 min	0.53	0.47	0.45
160 min	0.57	0.43	0.41
320 min	0.57	0.43	0.41
640 min	0.57	0.43	0.41
1280 min	0.55	0.45	0.42

T. Hofmann, editors, *Advances in Neural Information Processing Systems*, volume 19, pages 785–792. MIT Press, Cambridge, MA, 2007.

- [10] P. Gao, A. Honkela, M. Rattray, and N. D. Lawrence. Gaussian process modelling of latent chemical species: applications to inferring transcription factor activities. *Bioinformatics*, 24(16):i70–i75, Aug 2008.
- [11] A. Honkela, C. Girardot, E. H. Gustafson, Y.-H. Liu, E. E. M. Furlong, N. D. Lawrence, and M. Rattray. Model-based method for transcription factor target identification with limited data. *Proc Natl Acad Sci U S A*, 107(17):7793–7798, Apr 2010.
- [12] P. Glaus, A. Honkela, and M. Rattray. Identifying differentially expressed transcripts from RNA-seq data with biological variation. *Bioinformatics*, 28(13):1721–1728, Jul 2012.
- [13] C. wa Maina, A. Honkela, F. Matarese, K. Grote, H. G. Stunnenberg, G. Reid, N. D. Lawrence, and M. Rattray. Inference of RNA polymerase II transcription dynamics from chromatin immunoprecipitation time course data. *PLoS Comput Biol*, 10(5):e1003598, May 2014.
- [14] C. G. Danko, N. Hah, X. Luo, A. L. Martins, L. Core, J. T. Lis, A. Siepel, and W. L. Kraus. Signaling pathways differentially affect RNA polymerase II initiation, pausing, and elongation rate in cells. *Mol Cell*, 50(2):212–222, Apr 2013.
- [15] S. Duane, A. D. Kennedy, B. J. Pendleton, and D. Roweth. Hybrid Monte Carlo. *Physics Letters B*, 195(2):216–222, 1987.

- [16] S. Hao and D. Baltimore. The stability of mRNA influences the temporal order of the induction of genes encoding inflammatory molecules. *Nat Immunol*, 10(3):281–288, Mar 2009.
- [17] D. L. Bentley. Coupling mRNA processing with transcription in time and space. *Nat Rev Genet*, 15(3):163–175, Mar 2014.
- [18] A. R. Grosso, S. F. de Almeida, J. Braga, and M. Carmo-Fonseca. Dynamic transitions in RNA polymerase II density profiles during transcription termination. *Genome Res*, 22(8):1447–1456, Aug 2012.
- [19] F. Catania and M. Lynch. A simple model to explain evolutionary trends of eukaryotic gene architecture and expression: how competition between splicing and cleavage/polyadenylation factors may affect gene expression and splice-site recognition in eukaryotes. *Bioessays*, 35(6):561–570, Jun 2013.
- [20] S. Anders and W. Huber. Differential expression analysis for sequence count data. *Genome Biol*, 11(10):R106, 2010.
- [21] A. Gelman and D. B. Rubin. Inference from iterative simulation using multiple sequences. *Statistical Science*, 7(4):457–472, 1992.
- [22] B. Langmead, C. Trapnell, M. Pop, and S. L. Salzberg. Ultrafast and memory-efficient alignment of short DNA sequences to the human genome. *Genome Biol*, 10(3):R25, 2009.
- [23] M. D. Robinson, D. J. McCarthy, and G. K. Smyth. edgeR: a Bioconductor package for differential expression analysis of digital gene expression data. *Bioinformatics*, 26(1):139–140, Jan 2010.
- [24] C. E. Rasmussen and C. Williams. *Gaussian Processes for Machine Learning*. MIT Press, 2006.
- [25] N. Hah, C. G. Danko, L. Core, J. J. Waterfall, A. Siepel, J. T. Lis, and W. L. Kraus. A rapid, extensive, and transient transcriptional response to estrogen signaling in breast cancer cells. *Cell*, 145(4):622–634, May 2011.

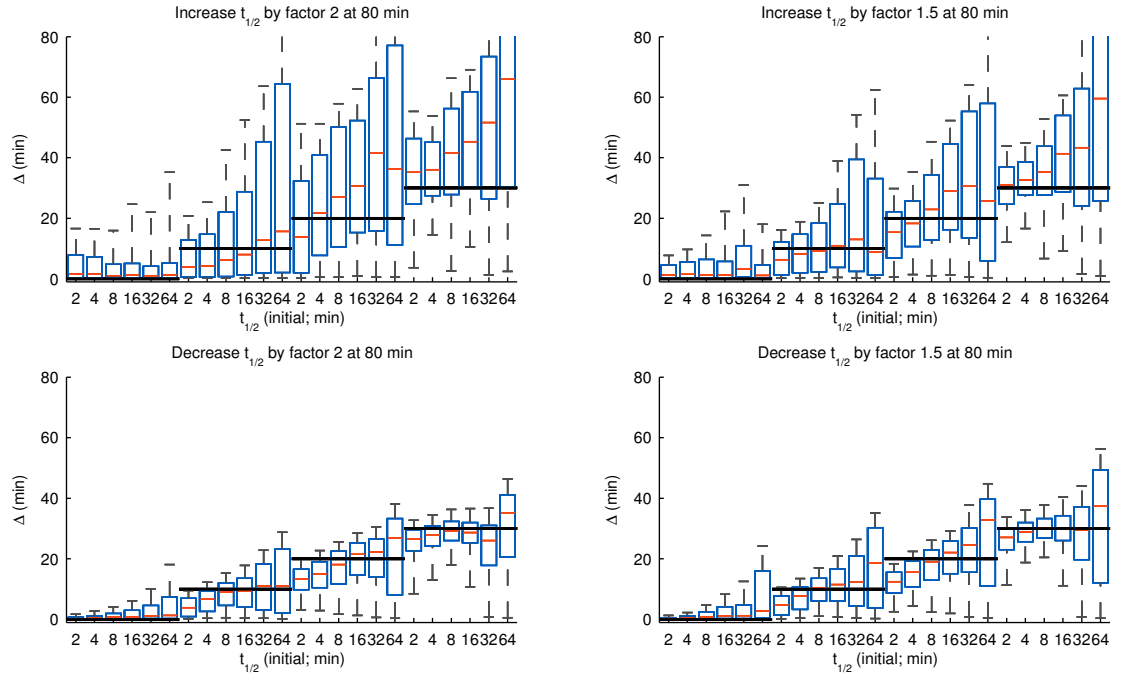


Figure S2: Boxplots of parameter posterior distributions illustrating parameter estimation performance on synthetic data for the delay parameter Δ . The strong black lines indicate the ground truth used in data generation. The box extends from 25th to 75th percentile of the posterior distribution while the whiskers extend from 9th to 91st percentile. This is a counterpart of Fig. 3 in a situation where the simulated mRNA half-life $t_{1/2}$ changes during the time course, something our model cannot capture. The simulated changes are point changes up or down with a factor of 1.5 or 2 at 80 min. The results show that delay estimates remain accurate and reliable, with the true value always in the high posterior density region, and demonstrate the conservativeness of the estimates with no sign of serious overestimation of small delays.

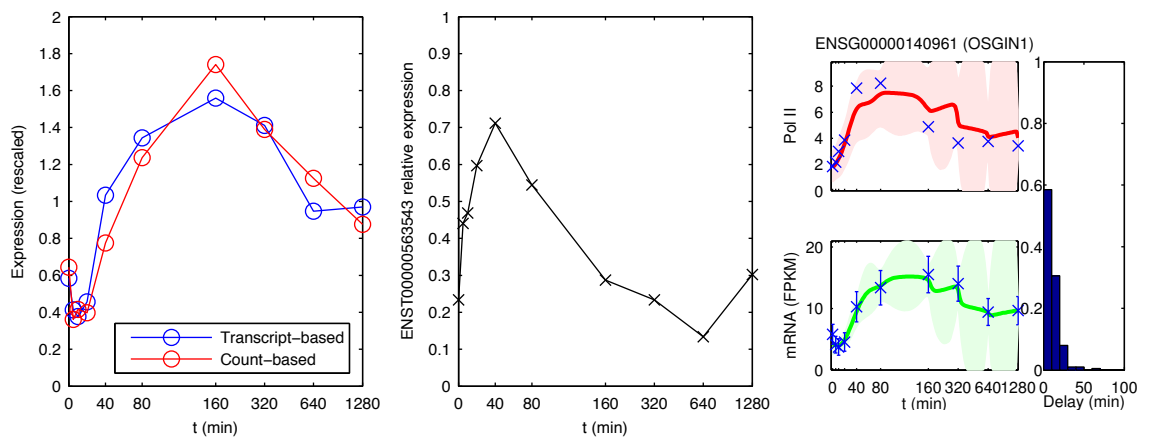


Figure S3: An illustration of how proper summarisation of the RNA-seq data is important for ruling out confounding effects from changing splicing patterns during the experiment. Left: Gene expression time series of the gene OSGIN1 from RNA-seq data using either transcript-based RNA-seq data summarisation as in the paper or using a simpler summarisation of counts of reads aligned uniquely to the mRNA transcripts of OSGIN1. Centre: Proportion of transcript ENST00000563543 out of all OSGIN1 transcripts. At 567 bp, this mRNA transcript is much shorter than the other major transcripts whose mRNAs are around 2 kb. Right: The model fit for OSGIN1 shows no evidence of significant delay, while the count-based profile in the left figure would suggest a longer delay.

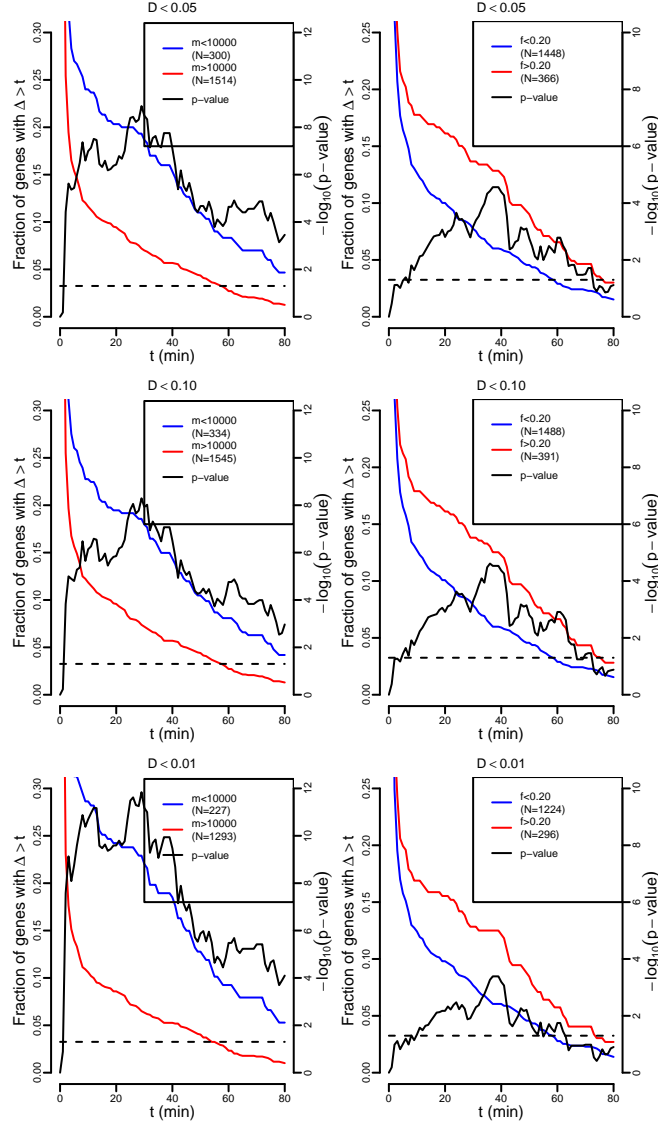


Figure S4: Alternative versions of Fig. 5 of the main paper: tail probabilities for delays for different cut-offs for D in Eq. (S29). Top: $D < 0.05$ (value used for main results), middle: $D < 0.1$, bottom: $D < 0.01$. Left: genes whose longest pre-mRNA transcript is short (m is the length from transcription start to end). Right: genes with relatively long last introns (f is the ratio of the length of the last intron of the longest annotated transcript of the gene divided by the length of that transcript pre-mRNA). The fraction of genes with long delays Δ is shown by the red and blue lines (left axis). In both subplots, the black curve denotes the p -values of Fisher's exact test conducted separately at each point (right axis) with the dashed line denoting $p < 0.05$ significance threshold. The general shapes of the curves are the same in every case.

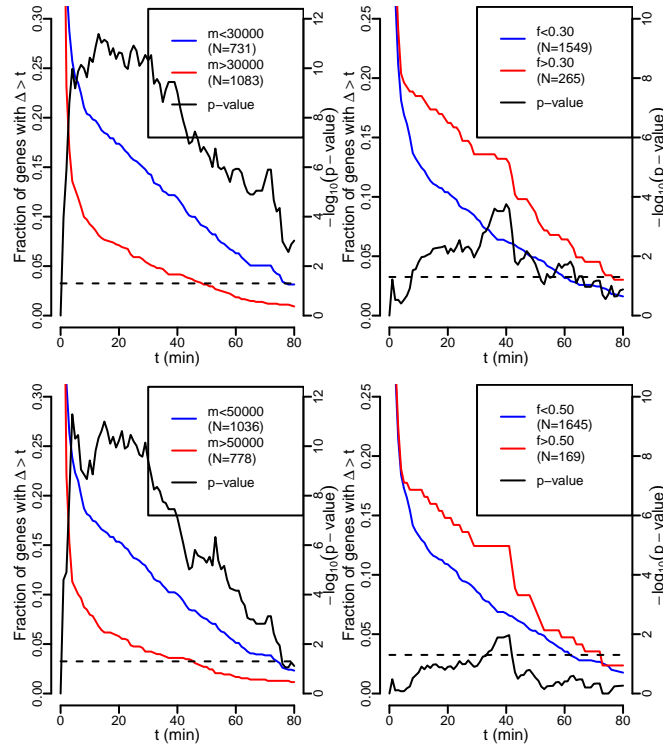


Figure S5: Alternative versions of Fig. 5 of the main paper: different cut-offs for f and m . Left: genes whose longest pre-mRNA transcript is short (m is the length from transcription start to end). Right: genes with relatively long last introns (f is the ratio of the length of the last intron of the longest annotated transcript of the gene divided by the length of that transcript pre-mRNA). The fraction of genes with long delays Δ is shown by the red and blue lines (left axis). In both subplots, the black curve denotes the p -values of Fisher's exact test conducted separately at each point (right axis) with the dashed line denoting $p < 0.05$ significance threshold. The general shapes of the curves are the same in every case.

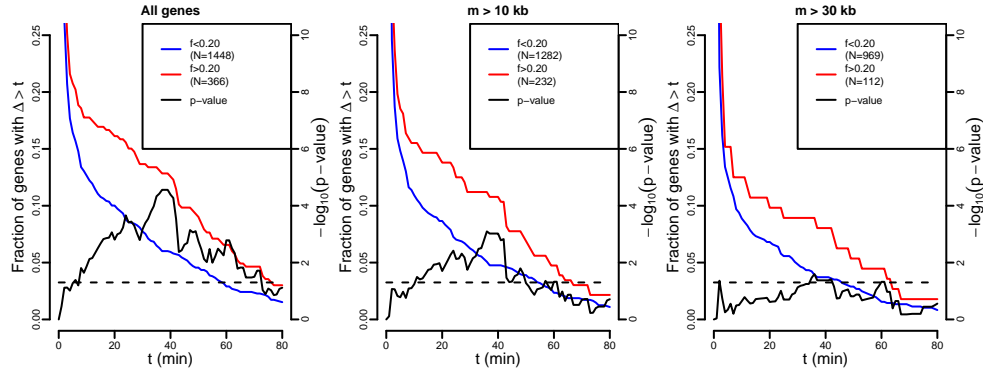


Figure S6: Alternative versions of Fig. 5 (right) of the main paper: explore the dependence on f for genes with a lower bound on mRNA length m . The fraction of genes with long delays Δ is shown by the red and blue lines (left axis). The black curve denotes the p -values of Fisher's exact test conducted separately at each point (right axis) with the dashed line denoting $p < 0.05$ significance threshold. The general shapes of the curves are the same in every case.

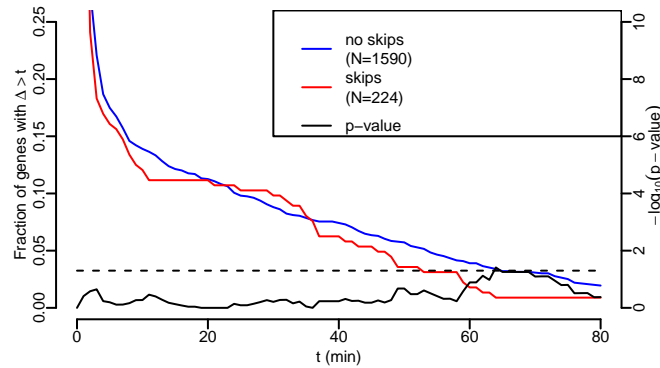


Figure S7: Proportion of long posterior median delays for genes with/without annotated exon skipping. The fraction of genes with long delays Δ is shown by the red (no skipped exons) and blue (skipped exons) lines (left axis). The black curve denotes the p -values of Fisher's exact test conducted separately at each point (right axis) with the dashed line denoting $p < 0.05$ significance threshold. There is no clear difference between the two groups.

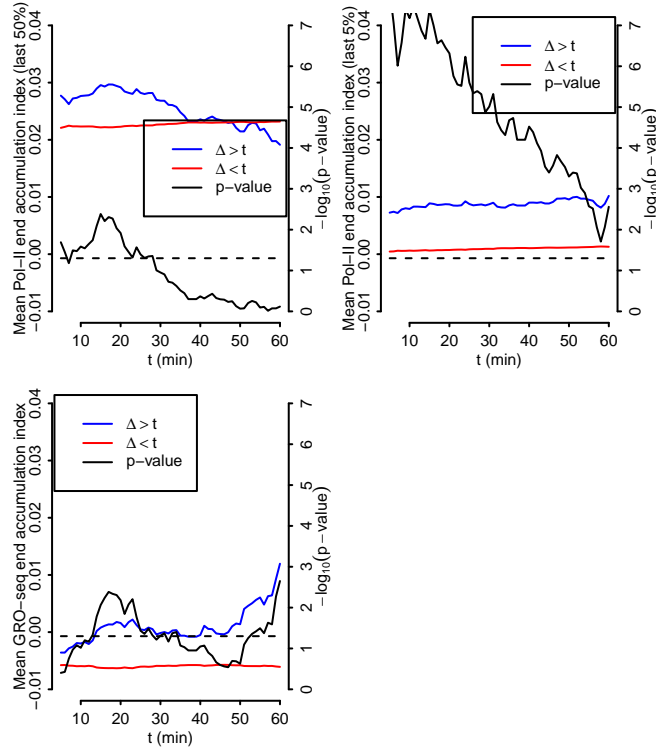


Figure S8: Alternative version of Fig. 6 (right) of the main paper: computing the index based on pol-II ChIP-seq and GRO-seq instead of intronic RNA-seq reads. The top plots show differences in the mean pol-II accumulation index in long delay genes (blue) and short delay genes (red) as a function of the cut-off used to distinguish the two groups (left axis). Positive values indicate increased pol-II accumulation at the 3' end (top left: last 50% of the gene body, top right: last 5% of the gene body) over time. The black line shows the p -values of Wilcoxon's rank sum test between the two groups at each cut-off (right axis). The bottom plot is the same as top right, except for GRO-seq data of [25], with the index is defined as the difference between the only late (160 min) time point and the average of the early (0-40 min) time points. In contrast to the pre-mRNA figure in the main paper, both long and short delay genes show a clear tendency towards accumulation of pol-II towards the end of the gene, but there is no clear difference between the two groups for the last 50% (top left), while there is a very consistent pattern of more pol-II accumulation very close to 3' end (top right) for long delay genes, and the level is essentially independent of the estimated delay. GRO-seq data in the last 5% (bottom) behave similarly as pol-II ChIP-seq (top right).

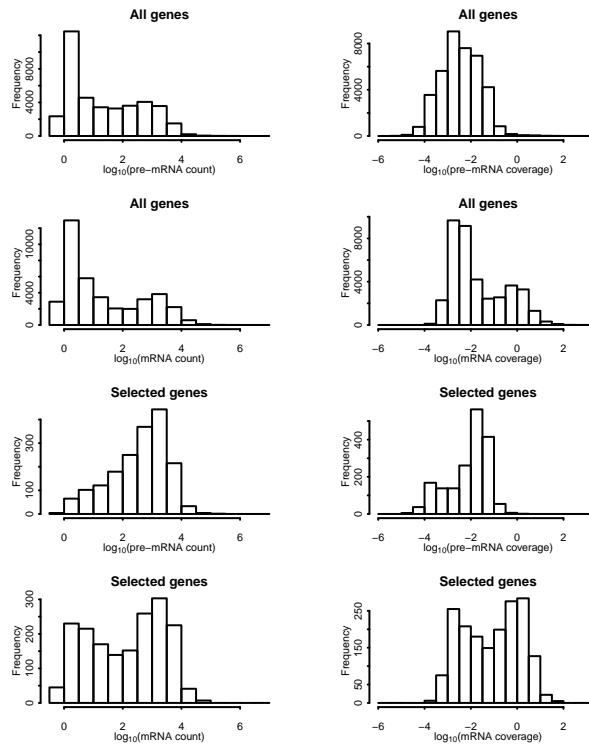


Figure S9: Distributions of per-gene mRNA and pre-mRNA counts and coverages based on BitSeq expression estimates. Top two rows show broad distributions for all genes, while the bottom two rows show distributions biased toward higher values for the selected 1786 genes. The results show that the mRNA coverages are mostly clearly higher than for pre-mRNA, again demonstrating a sensible split between pre-mRNA and mRNA.

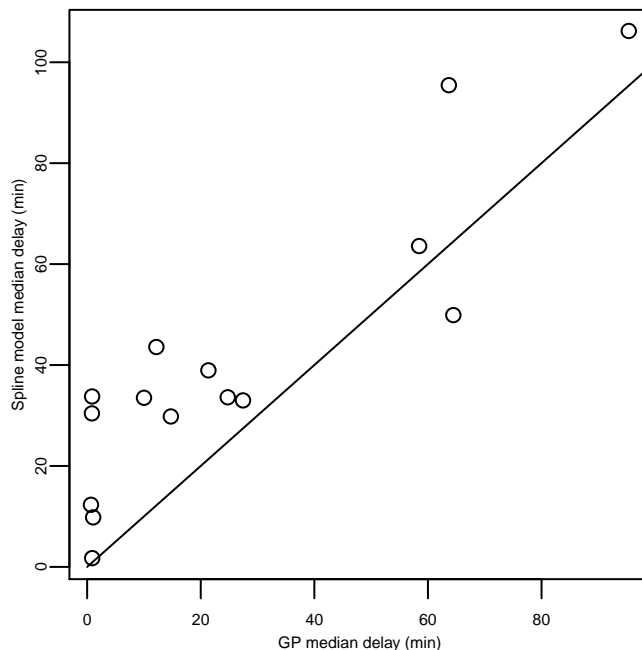


Figure S10: Comparison of estimated posterior median delays from the GP model with an alternative spline-based model for $n = 15$ genes with reliable estimates. In this model we used cubic smoothing splines to fit continuous curves to pol-II measurements. To account for the uneven sampling the times were transformed as $t' = \log(t/\text{min} + 5)$. The regularisation strength was shared over all genes and optimised by leave-one-out cross validation over all internal time points. The time transformation was also found to work much better than untransformed time in the cross validation. The smoothed pol-II curves were used as input to Eq. (S2) which was solved numerically to obtain predictions for $m(t)$. Assigning a Gaussian noise model to $m(t)$ similar to the GP model and using similar priors for all shared parameters, we run MCMC to obtain posteriors over the parameters. We were only able to obtain reliable parameter estimates for a small subset of genes for which the method had a good fit (measured through expected relative residual variance) for both pol-II and mRNA. The other estimates were unreliable presumably because the method estimated the pol-II profiles independently but then ignored the uncertainty related to this estimation, which further highlights the benefits of the GP approach.

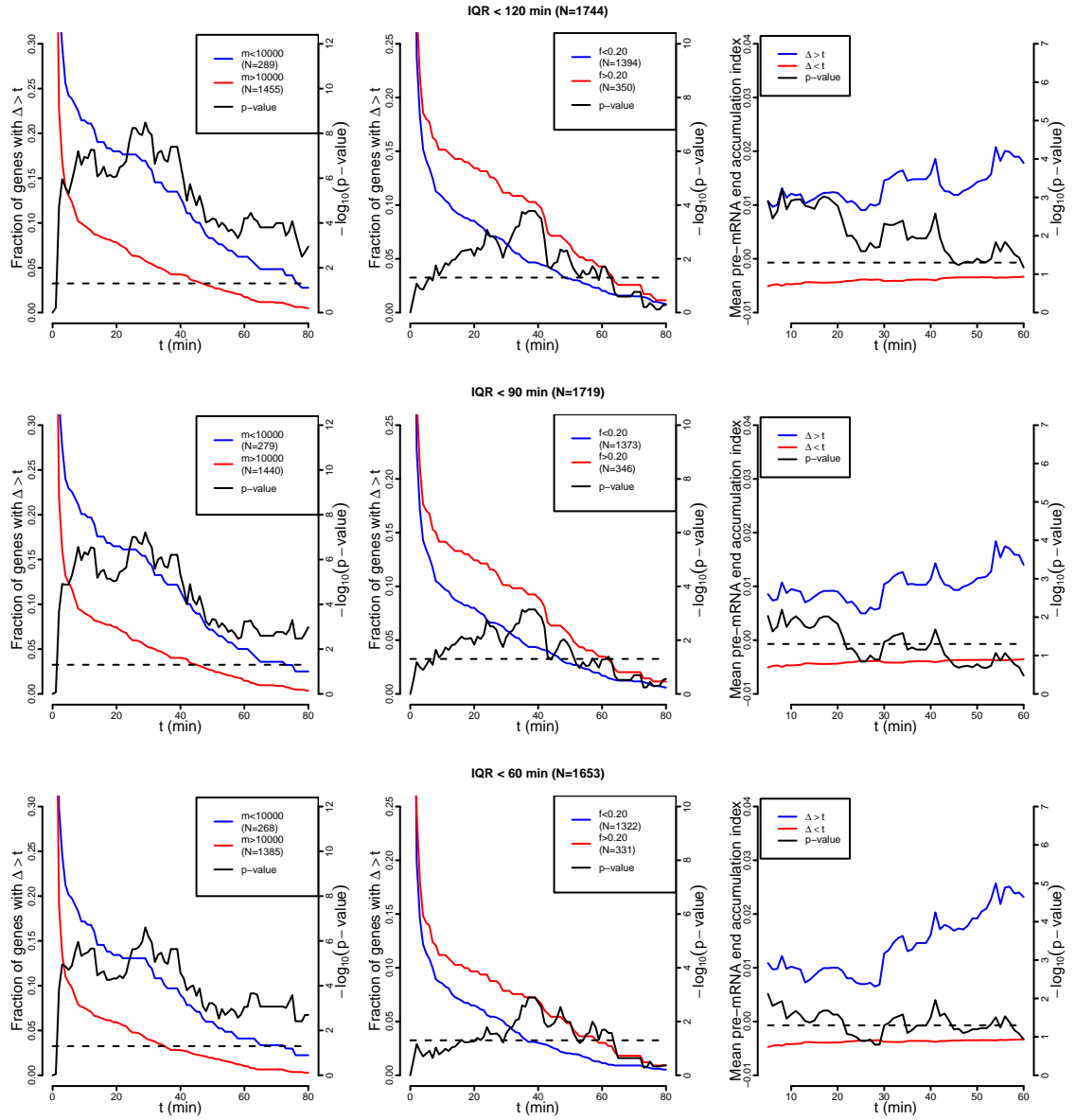


Figure S11: Alternative versions of Figs. 5 and 6 under more stringent filtering of delay posterior interquartile range (IQR).